# Broad-Band Imaging of a Large Sample of Irregular Galaxies

Deidre A. Hunter

Lowell Observatory, 1400 West Mars Hill Road, Flagstaff, Arizona 86001 USA

dah@lowell.edu

and

Bruce G. Elmegreen

IBM T. J. Watson Research Center, PO Box 218, Yorktown Heights, New York 10598 USA

bge@watson.ibm.com

#### ABSTRACT

We present the results of UBV imaging of a large sample of irregular galaxies: 94 Im systems, 24 Blue Compact Dwarfs (BCDs), and 18 Sm galaxies. We also include JHK imaging of 41 of these galaxies. The sample spans a large range in galactic parameters. Ellipse fit axial ratios, inclinations, and position angles are derived, integrated photometry and azimuthally-averaged surface photometry profiles are determined, and exponential fits give the central surface brightnesses, scale lengths, and isophotal and half-power radii. These data are used to address the shapes of Im galaxies, look for clues to past interactions in large-scale peculiarities, examine the nature and consequences of bars, study color gradients and large-scale color variations, and compare the exponential disk profiles of the young and old stellar components. For example, color gradients exhibit a great variety and not all passbands are correlated. Bars are associated with higher star formation rates. Many irregulars show a double exponential radial light profile that is steeper in the outer parts, and these are reproduced by a new model of star formation that is discussed in a companion paper. Some galaxies, primarily BCDs, have double exponentials that are steeper (and bluer) in the inner parts, presumably from centralized star formation. Im-types have thicker, lessprominent dust layers than spiral galaxies because of their lower average surface densities and midplane extinctions.

Subject headings: galaxies: irregular— galaxies: fundamental parameters—

stars: formation

### 1. Introduction

Dwarf irregular (dIm) galaxies serve as laboratories of star formation without the influence of spiral density waves or shear. They have evolved relatively slowly over time and chemically resemble the outer parts of present-day spirals. Ultra-low surface brightness dIms may represent the slowest evolving galaxies in the Universe. If dIms evolve via periodic starbursts, then they could dominate intermediate redshift surveys. They are so numerous and contain such a large fraction of their mass in gas, that the most distant dwarfs may dominate the faint QSO absorption lines. They are like the proposed building blocks of spiral galaxies in the cold dark matter theory. For all of these reasons, dIm galaxies are an important component of the Universe.

Normal dIm galaxies span a range of a factor of 10<sup>4</sup> in star formation rate per unit area, yet detailed studies of their stellar populations suggest that most evolve with a star formation rate that varies by only a factor of a few over time (Ferraro et al. 1989; Tosi et al. 1991; Greggio et al. 1993; Marconi et al. 1995; Gallart et al. 1996a,b; Aparicio et al. 1997a,b; Dohm-Palmer et al. 1998, Gallagher et al. 1998, Gallart et al. 1999). Some show evidence of higher amplitude variations, however (Israel 1988, Tolstoy 1996, Dohm-Palmer et al. 1997, Greggio et al. 1998, Tolstoy et al. 1998). What distinguishes dwarf galaxies with high star formation rates from those with low rates? We believe this variation, which is also present to a lesser extent in spirals (Kennicutt 1989; Rocha-Pinto et al. 2000), indicates there is a fundamental aspect of star formation that is missing from the current theory.

What governs star formation locally within a galaxy is also not clear. Dense, star-forming clouds and H II regions form near the central regions, yet the detectable stars extend far beyond this, with the gas going out further still. Does star formation also occur in the outer disk but without showing prominent H II regions?

In a differentially-rotating disk there is a critical column density  $\Sigma_c$  above which the disk is unstable to ring-like perturbations in the radial direction (Toomre 1964). Kennicutt (1989) and Martin & Kennicutt (2001) determined the analogous column density for star formation using a sample of Sc spiral galaxies. They found that the ratio of observed gas density  $\Sigma_g$  to critical gas density  $\Sigma_c$  has a characteristic value at the radius where significant star formation ends. Presumably gas is too stable to form stars further out.

Motivated by the success of the Toomre gravitational instability model for spiral galaxies, we and others applied it to dIm galaxies (Hunter & Plummer 1996; Meurer et al. 1996; van Zee et al. 1997a; Hunter, Elmegreen, & Baker 1998). The results suggested that dIms should not be forming stars at all: most have  $\Sigma_g < \Sigma_c$  throughout. The model also fails to predict where star formation ends or which galaxies have higher rates. A related result was

found for spiral galaxies: stars continue to form beyond the radius where the gas surface density drops below the threshold (Ferguson et al. 1998). These results implied that processes other than large-scale spontaneous instabilities are important in tiny galaxies and the outer parts of spiral galaxies, leading us to examine more local effects. These include triggering from supernovae and other stellar pressures and gravitational collapse following turbulence compression (see review by Mac Low & Klessen 2004). Also likely to be important is the thermal state of the gas, that is, whether cool clouds can form at the local pressure and radiation field (e.g., Elmegreen & Parravano 1994; Wolfire et al. 2003; Schaye 2004).

In a study of the dIm NGC 2366 (Hunter, Elmegreen, & van Woerden 2001a), we found that star formation occurs primarily where the gas column density exceeds 6  $M_{\odot}$  pc<sup>-2</sup> (also see van der Hulst et al. 1993; van Zee et al. 1997a; Meurer et al. 1998). This threshold corresponds approximately to the presence of a cool phase of HI, which may be a second requirement for star formation. We also found that the peak densities in regions of star formation are equal to the local tidal densities for gravitational self-binding of a co-rotating cloud against galactic tidal forces. This binding condition may be more fundamental than the Toomre condition because it is local, 3-dimensional, and does not involve ring or spiral arm generation as an intermediate step toward star formation.

To address the question of what regulates star formation in tiny galaxies, we have conducted a multi-wavelength survey of a large sample of reasonably normal, relatively nearby galaxies without spiral arms. The data consist of UBV and H $\alpha$  images for the entire sample, and JHK images, H I maps, CO observations, and H II region spectrophotometry for a sub-sample. The H $\alpha$ , UBV, and JHK image sets act as probes of star formation on three different times scales: H $\alpha$  images trace the most recent star formation ( $\leq$ 10 Myrs) through the ionization of natal clouds by the short-lived massive stars; UBV, while a more complicated clue, is dominated by the stars formed over the past Gyr for on-going star formation (Gallagher et al. 1984); and JHK integrates over the lifetime of the galaxy (Hunter & Gallagher 1985a).

So far, we have used these data to conduct several case studies (NGC 2366: Hunter, Elmegreen, & van Woerden 2001a; DDO 88: Simpson, Hunter, & Knezek 2005a; DDO 43: Simpson, Hunter, & Nordgren 2005b) as well as studies of the H II region luminosity function and distributions (Youngblood & Hunter 1999, Roye & Hunter 2000), gas abundances (Hunter & Hoffman 1999), pressures of H II regions relative to the background galactic disk (Elmegreen & Hunter 2000), and V-band and H $\alpha$  power spectra (Willett, Elmegreen, & Hunter 2005). The H $\alpha$  data of the entire sample were presented previously (Hunter & Elmegreen 2004). Here we present the UBVJHK imaging data of the full sample.

# 2. The Sample

The 136 sample galaxies are listed in Table 1 where we have grouped the galaxies into three categories: Im—94 systems, Blue Compact Dwarf (BCD)—24 systems, and Sm—18 systems. The morphological classifications were taken from de Vaucouleurs et al. (1991=RC3). Irregular galaxies were first described by Hubble (1926) as "lacking both dominating nuclei and rotational symmetry" with the "Magellanic Clouds [as] the most conspicuous examples." The Sm class was created when de Vaucouleurs (1959) described an extension of "the spiral sequence into the irregular types" which he noted as "SBd or SBm." This extension was motivated by the "recognition of spiral structure in the Magellanic Clouds and objects of similar type" (de Vaucouleurs 1954). The Sm class was later described by de Vaucouleurs (1963) as "the transition stage toward the Magellanic irregulars Im (whether barred or not)."

The BCD class is not part of the RC3 morphological system, but rather was imposed on galaxies after the identification of compact, high surface brightness "HII galaxies" that are dominated by nebular emission lines (Sargent & Searle 1970). Some BCDs have properties similar to those of Im systems (Kunth 1985). To select BCDs that are comparable to the Im galaxies we used the width at 20% intensity of the integrated HI profile  $W_{20}$  to select systems that are comparable in mass to Im systems ( $W_{20} \le 175 \text{ km s}^{-1}$ ).

The galaxies were chosen to be relatively nearby, and biased to systems containing gas. The sample is not complete, but it spans a large range in galactic parameters and is representative. The galaxy characteristics include a range in integrated luminosity ( $M_V$  of -9 to -19), average surface brightness (20 to 27 mag/arcsec<sup>2</sup>), current star formation activity (0 to 1.3  $M_{\odot}$  yr<sup>-1</sup> kpc<sup>-2</sup>), and relative gas content (0.02 to 5  $M_{\odot}$  /L<sub>B</sub>). A more complete description of the sample and of its selection is given by Hunter & Elmegreen (2004) where we present the H $\alpha$  imaging data. Four galaxies observed in H $\alpha$  are not included here because we do not have broad-band imaging of them (NGC 1705, NGC 2101, NGC 3109, F567-2), and two additional galaxies (DDO 125 and Mrk 67) have been dropped because they are interacting with companions. On the other hand, two galaxies without H $\alpha$  imaging are added to the broad-band imaging sample (F473-V1 and F620-V3).

The distances to the galaxies in our sample and references from which the distances are taken are given in Table 1. We used distances determined from variable stars or the tip of the Red Giant Branch, if they were available. Other distances were determined from the radial velocity relative to the Galactic standard of rest  $V_{GSR}$  (RC3) and a Hubble constant of 65 km s<sup>-1</sup>Mpc<sup>-1</sup>. While this might not be the most modern version of the Hubble constant and we do not correct for Virgo-infall, we have retained the distances that were used in the presentation of the H $\alpha$  survey data (Hunter & Elmegreen 2004) and in several

papers presenting HI data (Simpson et al. 2005a,b) so that combining data from the various wavelengths is straightforward. Two galaxies—F473-V1 and F620-V3—have no distance determination.

For comparison to spiral galaxies we have used the sample compiled by Kennicutt (1983). This sample of 74 galaxies spans the range of morphologies from Sab to Sd. Kennicutt has measured H $\alpha$  fluxes for these galaxies. Other properties were obtained from RC3 and Fisher & Tully (1981). For the spirals,  $\mu_{25}$ , the average B-band surface brightness within an isophote of 25 magnitudes in 1 arcsec<sup>2</sup> (discussed below in Fig. 6), has been converted from the value in the RC3 to one that matches the definition of surface area used here, i.e. the area of the projected ellipse used for the denominator of the surface brightness calculation in the RC3 has been replaced here with the area of the circle having a radius equal to the semimajor axis.

Foreground reddening  $E(B-V)_f$  was determined from Burstein & Heiles (1984) and values are given in Table 1. The reddening law of Cardelli, Clayton, & Mathis (1989) was adopted with  $A_V = 3.1 \times E(B-V)_t$ , where the total  $E(B-V)_t$  is that due to foreground plus internal reddening. An internal reddening correction of  $E(B-V)_i = 0.05$  was adopted for all sample galaxies.

For the Kennicutt (1983) sample of spirals, an extinction correction was made to face-on orientation using the formulation of Tully et al. (1998) and the minor-to-major axis ratios given by RC3. We then adopted a face-on internal  $E(B-V)_i^0$  of 0.2 mag. Note that this is a change from our treatment of spirals in Hunter & Elmegreen (2004) where we adopted a single internal reddening of 0.3 mag after Kennicutt (1983) with no correction based on inclination. For 8 spirals the difference compared to our previous treatment is an increase in  $E(B-V)_t$  of 0.1–0.2 mag, and for 4 spirals the increase is as high as 0.5 mag. But for the other 63 galaxies the change is less than 0.1 mag, sometimes to a greater reddening correction and sometimes to a smaller correction.

### 3. The images

### 3.1. UBV

UBV images of our sample galaxies were obtained by one of us (DAH) in 27 observing runs, all but two of which took place 1997 to 2002. The observations are listed in Table 2. Most galaxies were observed in U, B, and V, but three have only B and V and 6 have only V images. One galaxy is shown in Figure 1 for illustration. All of the data are available from http://www.lowell.edu/users/dah/images/, and a few UBV color images constructed from

the UBV can be seen at http://www.lowell.edu/users/dah/ubv.html.

Most of the observations were made with a SITe  $2048 \times 2048$  CCD binned  $2 \times 2$  on either the Lowell Observatory 1.1 m Hall Telescope or the Lowell Observatory 1.8 m Perkins Telescope. Three galaxies—F565-V2, F563-V1, and F561-1—were observed with a TI  $800 \times$ 800 CCD on loan from the U. S. Naval Observatory, Flagstaff Station coupled with a 4:1 focal reducer. In most cases several images were obtained of each galaxy in each filter. The telescope position was usually offset 20" between each observation in order to average over flat-fielding defects. The electronic pedestal was subtracted using the overscan strip, and the images were flat-fielded using twilight sky flats. The counts in the twilight sky flats were high enough that they contribute much less than 1% uncertainty to the galaxy images. Landolt (1992) standard stars were used to calibrate the photometry. For some galaxies observed on cloudy nights, frames of the galaxy were taken on separate clear nights for purposes of calibration. The multiple images of a galaxy in each filter were aligned and averaged with an algorithm to eliminate cosmic rays but preserve the photometric integrity of the image. The scale, seeing (FWHM of isolated star profiles), and rms of the photometric calibration of the final images are given in Table 2. The uncertainty in the calibration is not included in the photometric uncertainty of extracted quantities.

A few galaxies were kindly imaged for us by P. Massey using the Kitt Peak National Observatory (KPNO) 4 m Telescope and either a 2048×2048 Tektronix CCD or the NOAO CCD Mosaic Imager, an array of 8 2048×4096 SITe CCDs. In the case of the Mosaic Imager, the galaxy was centered on and completely contained within one of the CCDs. For the Mosaic Imager, dome flats and twilight sky flats were used to remove the pupil ghost as well as determine the pixel-to-pixel variations. The images were corrected for geometrical distortions and stacked to produce a single final image in each filter. (See Massey and collaborators' "Local Group Survey: Mosaic Reduction Notes" at http://www.lowell.edu/users/massey/lgsurvey/splog2.html for details on how they have reduced Mosaic Imager data). The Mosaic Imager data were calibrated using field images and standard stars observed at the Lowell Observatory 1.1 m Telescope. P. Massey also obtained B and V images of IC 1613 for us with the Cerro Tololo InterAmerican Observatory (CTIO) Curits Schmidt 61 cm Telescope and a SITe 2048 × 2048 CCD.

In addition, Sextans A was observed by us with the CTIO 0.9 m Telescope and these data are described by Hunter & Plummer (1996). IC 4662 and DDO 214 images were obtained with the CTIO 1.5 m and reported by Hunter et al. (2001b). We also observed DDO 214 at Lowell Observatory, and we have treated the two sets of observations of DDO 214 separately for purposes of comparing photometry and other derived parameters. However, the images obtained at Lowell Observatory go deeper and are preferred for that reason, while the CTIO

observations include U. Images of NGC 6822 were taken by C. Claver with the Prime Focus Direct Imager on the CTIO 4 m Telescope and a Tektronix  $2048 \times 2048$  CCD. These data were calibrated with images obtained with the Lowell Observatory 1.1 m Telescope. Finally, V-band images of Haro 3 were obtained as part of Service Observing on the KPNO 0.9 m Telescope with a Tektronix  $2048 \times 2048$  CCD.

Before performing surface photometry, we edited foreground stars and background galaxies from the final UBV images, interpolating across the edited region. Usually, the V-band image was done by hand, and then the cursor log file produced from that was used to remove objects from the other two filters. In that way, objects were removed in the same manner from each filter. One uncertainty in the galaxy surface photometry of the outer regions is in distinguishing galactic from other objects.

We then made a two-dimensional non-linear fit to the background and subtracted it from the image to produce a sky-subtracted final image for analysis (after Bell et al. 2000a and de Jong & van der Kruit 1994). Sky subtraction is an important source of uncertainty in our surface photometry. Therefore, to gain confidence in our results, we have explored the uncertainty in the sky. First, we computed half of the difference between the maximum and minimum in the fit to the sky over the images (not just in the region of the galaxy but excluding a border around the edges of the images). The average in this quantity is 1.2% of the sky. This is the contribution to the uncertainty that would result if we did not remove the large-scale variation at all, and obviously we have done better than that by fitting and subtracting the background. Second, we have taken the uncertainty of the sky from Poisson statistics of the sky counts (formula given in §3.3): the square-root of the sky counts times the gain of the CCD. For each of our images the Poisson statistics yields a greater uncertainty - an average of 2.2% per pixel - than those from the difference between the maximum and minimum in the sky fit. Thus, we assume that our sky uncertainty is dominated by Poisson statistics, especially after removal of the large-scale variations, and Poisson statistics is the uncertainty that we use throughout this paper. Using this uncertainty gives us confidence in the results that stand out above the sky. This confidence will be important in our discussion of outer disk profiles, where the galaxy intensity is far below the sky intensity but well above the uncertainty of the sky intensity. The average Poisson variation in the galaxy counts, combined with the average uncertainty in the sky fit, suggests that the average uncertainty in the photometric measurement of our galaxies is of order 0.02–0.03 mag.

### 3.2. JHK

JHK images of 41 galaxies in our sample (26 Im, 12 BCD, and 3 Sm) were obtained by one of us (DAH) in 9 observing runs 1996 February to 1998 May. Seventeen galaxies were observed in only J or, in the case of DDO 35, only H. Twelve galaxies were observed in J and H, and 12 in J, H, and K. The observations are listed in Table 2. One galaxy is shown in Figure 1 for illustration. All of the data are available from http://www.lowell.edu/users/dah/images/. These images were obtained using the Ohio State Infrared Imager-Spectrograph (OSIRIS) on the Perkins 1.8 m Telescope. The instrument consisted of four mosaiced detectors to create a total array of 256×256 pixels. Observations were made with a pixel scale of 1.50" for a total field of view of 6.4'.

Zero-second dark frames were subtracted from all of the data, the image pixel values were corrected for non-linearity effects, and pixel-to-pixel sensitivity variations were removed using observations of a white screen in the dome. Since OSIRIS consists of four detectors, separate linearity corrections were determined for and applied to each quadrant of an image. Non-linearity was of order 3% at levels of 15,000 counts. We took images of the white screen in the dome both with and without the screen illuminated, and subtracted the latter from the former in order to remove stray background light before forming the flat-field correction.

Observations of the galaxies consisted of several integrations of approximately 5, 10, and 20 seconds for K, H, and J-bands, respectively. For large galaxies that occupied most of the field of view, the telescope was moved about 5' away for sky observations every few minutes or less. Periodically the direction and length of throw to sky were varied, and the center of the galaxy was moved around in steps of 10". The purpose of these steps was to allow the pattern of stars in the sky observation and the locations of hot pixels relative to the galaxy to change so that they could be removed. For small galaxies, the telescope was nodded between images to place the galaxy alternately on one-half of the array and then the other, allowing sky to be determined while also observing galaxy. The object frames were sky-subtracted, aligned, and averaged.

"UKIRT" standard stars from the list compiled by S. Courteau were used to calibrate the photometry, and so the photometry is on the UKIRT system. The California Institute of Technology (CIT) photometric system is 8% bluer in J-H and 4% bluer in H-K compared to the UKIRT system. Each star was observed 4 times with the star placed in each quadrant of the detector array in turn, and sky for a specific observation was taken from the observations with the star in the other quadrants. We checked our photometry by comparing with the IR photometer observations of NGC 4449 made by Hunter & Gallagher (1985a) with a 16" aperture. Our imaging data yielded J and H magnitudes that were 0.24 magnitudes brighter than those obtained by Hunter and Gallagher, but the J-H color difference was zero.

We observed a few spiral galaxies in JHK for comparison. These include NGC 3274 (SABd?), NGC 4027 (SB(s)dm), NGC 4684 (S(r)B0+), NGC 4800 (SA(rs)b), and UGC 2984 (SBdm+). We did not obtain UBV observations for these systems. In addition, we observed the H II region NGC 5471 in M101 and the globular cluster NGC 6229 for examples of a very young and a very old stellar population, respectively.

### 3.3. Surface photometry

Surface photometry was performed on all of the broad-band and H $\alpha$  images. Because Im galaxies are lumpy, automatic ellipse fitting routines seldom perform well on these galaxies. Therefore, we determined the center of the galaxy, position angle, and ellipticity from a contour in the outer half of the V image which was block-averaged by factors of a few to increase the signal-to-noise. The center is simply the geometrical center of this isophote and the major axis is the longest bisector that passes through the center that, as much as possible, symmetrically divides the galaxy. One exception was DDO 40 for which an inner contour was used instead because the outer extended starlight did not seem to fairly represent the bulk of the galaxy.

We then fixed these parameters and integrated in ellipses that increase in semi-major axis length in approximately 10'' steps. The center, position angle (P.A.), minor-to-major axis ratio b/a, and ellipse step size are given in Table 2. Bad pixels due to unsubtracted or poorly subtracted foreground stars, satellite trails, or other flaws were masked and not used in the photometry. The flux in each ellipse was scaled from the actual area used to the expected area of the ellipse to account for such masked pixels. In the cases of DDO 143, Haro 36, and Mrk 16, much of the galaxy image was obliterated by a very bright nearby star.

Since we wished to compare the surface brightness photometry between these various images, we geometrically transformed the UBJHK and H $\alpha$  images to match the V image and used the same elliptical integration parameters as were used for V. The exception was that in a few cases H $\alpha$  required more ellipses (see especially, NGC 1569).

The surface photometry was fit with  $\mu = \mu_0 + 1.086R/R_D$  which represents an exponential disk and  $R_D$  is the scale-length of the disk. The range of radii to fit was determined for each galaxy from examination of a plot of  $\mu_{V_0}$  or  $\mu_{J_0}$  as a function of radius. Deviations from a linear relation in the center or in the outer parts or excursions due to a very large star-forming region as in NGC 2366 were excluded from the fit. The fit was made with uniform weighting of each radial data point. In some galaxies  $\mu_{V_0}$  is best fit with two lines

instead of one. In those cases, each fit was done separately, and, again, the range of radii to fit for each line was determined by examining the  $\mu_{V_0}(R)$  plot.

The relative uncertainty in the surface photometry at each annulus was determined assuming Poisson statistics, and is the sum of the squares of the uncertainties in the galaxy counts in each of the two ellipses that form the annulus and in the sky for each ellipse, divided by the galaxy counts in the annulus,  $f_a$ :

$$\sigma_{\mu} = \frac{1.086}{f_a} \sqrt{(f_2' + f_1' + 2s(A_1 + A_2))/g},\tag{1}$$

where subscript 1 and 2 refer to the first and second ellipses that bracket the annulus in question, f' is the sky-subtracted counts, s is the average sky per pixel in the image, A is the area of the ellipse in pixels, and g is the gain of the CCD. An example of our surface photometry is given in Figures 2 and 3. NGC 2366 was chosen for this example because it has a complete UBVJHK data set. Plots of all of the surface photometry can be obtained from http://www.lowell.edu/users/dah/sbplots.

Integrated photometry is given in Table 3. The integrated photometry is given at several different radii for each galaxy, including the half-light radius  $R_{1/2}^V$  and radii appropriate to the JHK images. Usually, K does not go as deep as H; H as deep as J; or J as deep as V. Therefore, photometry values are reported at the maximum extents for reasonable uncertainties in each of the JHK passbands. The largest radius listed is the maximum extent of the V-band measurements.

In Table 4 we report various structural parameters measured from the surface photometry. This includes the exponential disk fits to both V (first line) and J (second line), if available. Some galaxy profiles were best fit with two lines, rather than a single line. In these cases,  $R_D$  and  $\mu_0$  labeled as "Primary" are those derived from the fit to what we considered to be the part of the profile that represents the bulk of the underlying stellar disk. The second fit is labeled "Secondary."  $R_{Br}$  is the radius at which the two fits cross, and the column labeled "Sec?" tells whether the secondary fit is to the outer part of the profile ("O") or to the inner profile ("I"). In the case of the BCDs, we have assumed that the inner part of the disk is dominated by the intense star formation there and so the outer galaxy is a truer representation of the underlying stellar disk (see, for example, Noeske et al. 2003). In the case of the Im and Sm galaxies that do not have centrally concentrated and intense star formation, we take a change in the outer disk, which usually occurs at low surface brightness levels, to represent a deviation from the basic underlying stellar disk, as is seen in some spirals (Pohlen et al. 2002).

Double-exponential disks may contain important information concerning star formation processes in galaxies. A star formation model that reproduces this profile is suggested in a

companion paper (Elmegreen & Hunter 2005). Because breaks in surface photometry profiles at low light levels could be caused by over or under subtraction of sky, it is important to demonstrate that these breaks are not artifacts of data handling. First, we note that many of the breaks occur at relatively high surface brightness levels where small errors in the determination of sky do not have much effect.

Second, we have done ultra-deep imaging of three of our sample of Im galaxies in order to examine the outer parts of the disks in more detail (Hunter, Elmegreen, & Anderson 2006). Two of these galaxies show breaks in the surface photometry in our survey data presented here. The new data were taken with a different instrument on a different telescope and processed completely independently from the present survey. The resulting new surface photometry shows the same breaks at the same radii and surface brightnesses. The one galaxy in the deep-imaging sample that did not show a break in the present surface brightness profile also did not show a break in the new data.

Third, we have verified that the double exponentials are present in the data by making intensity cuts 11 pixels wide along the major axes of seven of the systems. Differences between the two sides of the galaxy are sometimes apparent in these cuts, which is to be expected for irregular galaxies. However, the break in the exponential profile is still clear on each side. This result implies that the azimuthal-averages used for the exponential fits in our full sample are not introducing false breaks that make them look like double exponentials. Such false breaks were suggested to be a possible source of smoothly tapering outer disk structure by van der Kruit (1988), who noted that edge-on galaxies usually have very sharp outer truncations. An example of an intensity cut from our data is illustrated for DDO 48 in Figure 4 along with cuts showing the original sky, the fit to the sky, and the background after sky subtraction. We conclude that the profile breaks and double-exponentials observed in our sample of galaxies are real features of the disk structures.

In Table 4 we report the radius at which the reddening-corrected B-band surface photometry reaches 25 mag in one arcsec<sup>2</sup>, R<sub>25</sub>, in the projected disk. We also give R<sub>H</sub>, the Holmberg radius, which was originally measured by Holmberg (1958) at a photographic surface brightness of 26.5 mag in 1 arcsec<sup>2</sup>. Here we have used the conversion from photographic magnitude to B-band magnitude listed in Table 11 of de Vaucouleurs et al. (1976; =RC2)  $\mu_B = 26.5 + 0.22 - 0.149(B - V)$ , where (B-V) is averaged over those radii where the color is well determined. For our galaxies this corresponds to a B-band surface brightness of between 26.60 and 26.72 mag in 1 arcsec<sup>2</sup> with an average of 26.64±0.002 mag in 1 arcsec<sup>2</sup>. We also list values of R<sub>1/2</sub>, the radius containing half of the V-band light of the galaxy.

In Table 5 we give  $\mu_{25}$ , the average B-band surface brightness within the isophote defined by  $R_{25}$ ;  $\mu_D^V$ , the average V-band surface brightness within the scale-length  $R_D^V$ ; and  $\mu_{2.5D}$ , the

average V-band surface brightness within the radius  $2.5R_D^V$ . These three surface brightnesses are not corrected for projection. They equal the galaxy flux divided by the area of the circle with a radius equal to the semi-major axis of the corresponding projected ellipse. This is in the convention of Holmberg (1958). In §4.2.3, we introduce another surface brightness,  $\mu_{2.5R_D}$ , which is the flux divided by the area of the isophotal ellipse whose semi-major axis equals  $2.5R_D^V$ . These two surface brightness definitions differ by the ratio of axes, with the latter value more appropriate for comparison with the survey surface brightness limit and models of apparent intensity. Finally, in Table 5 we also include the inclination of the galaxy i derived from b/a under the assumption that the intrinsic  $(b/a)_0$  of an edge-on Im system is 0.3 (Hodge & Hitchcock 1966; van den Bergh 1988).

# 3.4. Comparison with the literature

Various of the galaxies in our sample have also been observed by others (Im galaxies: Aparicio et al. 2000; Barazza et al. 2001; Bremnes et al. 1998, 1999, 2000; Carignan & Freeman 1988; Doublier et al. 1999; Karachentsev et al. 1999; Lee et al. 1999; Makarova 1999; Patterson & Thuan 1996; Thuan et al. 1999; van Zee 2000; BCD galaxies: Cairós et al. 2001,2003; Doublier et al. 2001; Noeske et al. 2003). This gives us the opportunity to check our measurements against those of others.

For 8 galaxies, our integrated U–B differ from those of others on average by  $0.5\sigma$  (0.04 mag); B–V for 23 galaxies differ by  $1.2\sigma$  (0.08 mag); and V by less than  $3\sigma$  (0.25 mag). Here  $\sigma$  is the quadratic sum of the uncertainties in our measurement and those in the literature. Results are similar for colors and magnitudes given by RC3. Our R<sub>25</sub>s differ on average from those given by RC3 by 0.4′, and R<sub>H</sub>s differ from those measured by Holmberg (1958) by 0.9′. The average surface brightness within R<sub>25</sub> given by RC3, and dereddened, differs from what we measure, converted to an elliptical area normalization, by 0.5 mag arcsec<sup>-2</sup> on average for 74 galaxies. From surface photometry, b/a is on average 4% different from those used by others for 24 galaxies, and the position angle differs by up to 40° for 33 galaxies. For 21 and 22 systems, our  $\mu_0^V$  and R<sub>D</sub> differ from others by  $4\sigma$  on average (0.9 mag and 19″, respectively).

Another useful comparison comes from the galaxy DDO 214 for which we obtained two sets of images, one with the Lowell Observatory 1.1 m Telescope and one with the CTIO 1.5 m Telescope. We treated these two data sets independently, although the Lowell Observatory data go deeper. The V magnitudes integrated over the galaxy differ by 0.06 mag, and B–V by 0.16 mag. The inferred b/a ratios differ by 0.04, or 5%, and the position angles by 4.5°. From surface photometry, the  $\mu_0^V$  differ by 0.18 mag arcsec<sup>-2</sup> (1.6 $\sigma$ ) and  $R_D^V$  by 3.6" (1.2 $\sigma$ ,

11%). The radii  $R_{25}$  and  $R_H$  differ by 1" (<1%, < 1 $\sigma$ ), and  $R_{1/2}^V$  by 2.6" (6%, < 1 $\sigma$ ). The  $\mu_{25}$  differ by 0.11 mag arcsec<sup>-2</sup>,  $\mu_D^V$  by 0.07 mag arcsec<sup>-2</sup>, and  $\mu_{2.5D}$  by 0.2 mag arcsec<sup>-2</sup>. Thus, except for B–V, the comparisons are reasonable. They suggest that an estimate of the total uncertainty in photometric quantities, including calibration (when not limited by Poisson statistics), is of order 0.03 mag, the same as we concluded in §3.1.

#### 4. Results

### 4.1. General Trends

Histograms showing the number distribution of the sample in  $M_{V_0}$ , the average B-band surface brightness within  $R_{25}$ ,  $\mu_{25}$ , and the average V-band surface brightness within  $R_D^V$ , are shown in Figures 5, 6, and 7. Figure 8 shows the number distribution of the sample in  $R_{1/2}^V$ , the radius that contains half of the light of the galaxy in the V-band.

# 4.2. General morphology

### 4.2.1. Peculiarities

Irregular galaxies are, of course, morphologically irregular. Even so, there is an orderedness to most Im systems. However, some irregular galaxies exhibit peculiar features that go beyond the norm for the class, and these are identified in Table 5. Several of the galaxies are curved or have crescent shapes: DDO 215 and F533-1. There are a few that have elongated structures extending from or curving around part of the galaxy (DDO 25, DDO 169, F620-V3, NGC 2552, UGC 5716, UGC 8276) that look like spiral-arm fragments or tidal tails. Others have broad, asymmetrical extensions (DDO 27, DDO 35, DDO 40, DDO 63, DDO 99, DDO 214, F651-2) or peculiar twists (DDO 48). One galaxy, DDO 165, has a sharp, curved southern edge. Some galaxies are simply messy with strong central regions and lower surface brightness scatter (DDO 9, DDO 34, DDO 68, UGC 199, UGC 8055, UGC 11820). In all, 18 of the 94 Im galaxies (19%) have noticeable large-scale morphological peculiarities, as do 5 of the 18 (28%) Sm systems. Oddly, none of the 24 BCD systems show these kinds of peculiarities even though the unusual intensity and pattern of star formation of the class suggest that these galaxies have incurred interactions. The sample with morphological peculiarities has the same distribution of current star formation rates as the rest of the sample, but tends to be bluer.

We have compared the position angles of the morphological major axis of the H<sub>I</sub> and

of the optical components of those survey galaxies with H I-line interferometric data in the literature. We eliminated galaxies with  $b/a \ge 0.9$  since the optical position angle is poorly determined when the image gets round. We have also eliminated galaxies with no clear rotation since the H I kinematical axis is then poorly determined. That left 31 Im and 6 Sm galaxies (no BCDs). Of these the majority have position angle differences that are less than 30°; seven galaxies have differences of 40–80°. Of these 7 galaxies, 3 are barred. Since bars can rotate with respect to the rest of the disk, a misalignment between the major axis of the bar and the outer disk is not unusual. The misalignment in the remaining 4 galaxies (DDO 26, DDO 53, DDO 86, DDO 168) may indicate a past disturbance. These galaxies, 13% of the Ims with H I interferometric data, are not marked as having morphological peculiarities, but the H I kinematics are also peculiar in two of them (DDO 26—Hunter & Wilcots 2002, DDO 168—Broeils 1992). These galaxies, combined with the fraction that show unusual morphological structures, mean that as many as one-third show some abnormality.

The most common phenomena that would account for these distortions to galaxy disks are interactions with other galaxies or extragalactic H<sub>I</sub> clouds. This is in spite of the fact that our sample is biased against obviously interacting systems. Dwarfs are also much more susceptible than giant spirals to disruption by the pressures of star formation. This follows from the low surface densities and interstellar pressures in dwarf galaxies, the lower levels of dust absorption at low metallicity, and the brighter uv fluxes from metal-poor massive stars. Interstellar turbulence at typical velocities should also be more disruptive in dwarfs than in spiral galaxies because the rotation speeds of the dwarfs are lower. When the turbulent speed is a large fraction of the rotation speed, the epicyclic radius becomes a large fraction of the disk scale. Then turbulent excursions that produce shells, holes, and cloud complexes are large compared to the disk scale-length, resulting in a more irregular overall appearance.

### 4.2.2. Bars

Some fraction of disk galaxies are barred, and irregular galaxies are no exception. However, identifying bar structures in irregular systems is harder than in spirals because the symmetry provided by spiral arms is missing. Furthermore, bars in Im galaxies can be comparable in size to the optical galaxy (NGC 1156: Hunter et al. 2002; NGC 2366: Hunter, Elmegreen, & van Woerden 2001a; NGC 4449: Hunter, van Woerden, & Gallagher 1999), so a large-scale boxy appearance due to a bar could be hard to distinguish from inclination effects. The contour plots that were used to determine the surface photometry parameters were also examined for the signs of a bar structure. A boxy appearance turning to rounder isophotes in the outer parts and/or a twisting of isophotes from the inner galaxy to the

outer galaxy were considered strong signs of a bar. Bar structures were often apparent in color-color ratio images as well, since many of the bars are blue and lined with H II regions.

If a galaxy appears to be barred, the bar length, minor-to-major axis length ratio, and change in position angle between the bar and the outer galaxy, if any, are given in Table 5. Characteristics of the bar were measured from a contour plot of the V-band image that was block-averaged by factors of a few to increase the signal-to-noise. The edge of the bar was taken to be the contour at which the shape ceased to be boxy and became more spherical and/or where the position angle changed. These changes were generally obvious but rarely sharp. The ambiguity in the end of the bar is quantified in the uncertainty in the bar's length.

In all, 22 of our 94 Im galaxies (23%) show evidence for a bar structure while 3 of 24 BCDs (12%) and 9 of 18 (50%) Sms do. Given the sample sizes, the percentage of BCDs and Sms with bars is not more than one sigma different from that of the Ims. The semi-major axis of the bar  $R_{Bar}$  relative to the disk scale-length  $R_D^V$  is shown in Figure 9.  $R_{Bar}$  is most often 1.5–2 $R_D^V$  for Im galaxies; the range is  $0.85R_D^V$  to  $3.5R_D^V$  and 7 of the 22 barred Im galaxies have  $R_{Bar}$  greater than  $2R_D^V$ . Thus, the bars in Im galaxies are relatively large, and in some cases occupy most of the optical galaxy. The bars in the Sm sample are smaller with a typical length of 1–1.5 $R_D^V$  and only one galaxy has a bar greater than  $2R_D^V$ . Bar minor-to-major axis ratios  $(b/a)_B$  range from 0.33 to 0.80 for Im galaxies with a typical value being 0.6–0.7. Bars in our Sm galaxies have similar shapes.

We have made profile cuts through the major and minor axes of the bars, centered on the optical center of the bar determined from the bar's outer isophotes in V. These profiles are illustrated in Figure 10. In some cases, the major and minor axes profiles are similar to each other, meaning that the bars are relatively thick. Most of the major axis profiles are exponential, as in late type galaxies in general (Elmegreen & Elmegreen 1985), but a few are flat, such as DDO 35, DDO 154 and DDO 133. There are no other obvious difference between these two cases.

Because of the spectacular offset bar in the nearby Im galaxy LMC, it is often assumed that bars in Im galaxies are generally offset from the galaxy centers. In our sample of barred galaxies, we found that the optical centers of the bars in 68% of the Im galaxies, 100% of the BCDs, and 67% of the Sms lie within 500 pc of the center of the galaxy defined by the outer V-band isophotes in the plane of the sky. Only 14% of the Ims (3 galaxies) and 22% of the Sms (2 galaxies) have bars whose centers lay more than 1 kpc from the optical center of the galaxy. The majority of Im galaxies with measurable offsets (57%, 8 galaxies) have offsets that are less than half of a disk scale-length. Only one has an offset that is greater than  $\mathbf{R}_D^V$ . The 4 Sm galaxies with measurable offsets lie between  $0.4\mathbf{R}_D^V$  and  $0.6\mathbf{R}_D^V$ . We conclude that

the offset feature of bars is not a general phenomenon of late-type galaxies.

Bars in Im galaxies appear to trigger a substantial amount of star formation. Figure 11 shows histograms of the integrated star formation rates, the average surface brightnesses inside  $R_D^V$ , and the ratios of the radial extents of the H II regions to  $R_D^V$  for the barred and unbarred samples. The medians for these three quantities, respectively, are  $-2.2 \text{ M}_{\odot} \text{ yr}^{-1} \text{ kpc}^{-2}$  (the logarithm of the integrated star formation rate normalized to the area within  $R_D^V$ ), 23.2 V-magnitude arcsec<sup>-2</sup>, and 3.0 for barred Ims, and  $-2.7 \text{ M}_{\odot} \text{ yr}^{-1} \text{ kpc}^{-2}$ , 24.1 V-magnitude arcsec<sup>-2</sup>, and 2.2 for non-barred Ims. Bars apparently increase the areal star formation rates and surface brightnesses by a factor of 2 to 3, and they increase the radial extents of the H II regions by a factor of  $\sim 1.4$ . This increase may simply reflect the increased density of gas in a bar compared to a non-barred central region, although gas shocking in a bar flow or gas pileup at the end of a bar could be additional triggers (Elmegreen & Elmegreen 1980). Slight shifts like these in star formation properties are also seen for BCD galaxies, but the statistics are too poor to make a conclusion. There is no obvious trend for the Sms.

# 4.2.3. Minor-to-major axis ratios

Past studies of the distributions of projected optical minor-to-major axis ratios b/a have derived the intrinsic shape of Im galaxies under the assumptions that there is one intrinsic shape and that galaxies are oriented at random on the sky. However, different studies have come to quite different conclusions. Hodge & Hitchcock (1966) and van den Bergh (1988) found that Im galaxies are modestly thick disks with an intrinsic ratio  $(b/a)_0$  of 0.3–0.4 rather than the 0.2 value generally adopted for spirals. Staveley-Smith, Davies, & Kinman (1992) suggested from gas kinematics that the disk is thicker than this, with  $(b/a)_0 \sim 0.6$ . On the other hand, Binggeli & Popescu (1995) and Sung et al. (1998) concluded that Im galaxies are triaxial in shape, similar to dwarf ellipticals.

The distribution of projected b/a for our sample of galaxies is shown in Figure 12. The statistical uncertainties are relatively low only for Im galaxies, which show a peak at b/a = 0.5 to 0.6. Although intrinsically flat, some edge-on Im galaxies might be misidentified as type Sm or even in some cases Sd. In any case, the decrease at low b/a in Figure 12 is consistent with an intrinsic thickness equal to  $\sim 0.3 - 0.4$  times the major axis length (Hodge & Hitchcock 1966; van den Bergh 1988). The decrease at large b/a could be caused by an intrinsically triaxial shape. The random projection of circular disks would give a flat distribution of b/a up to b/a = 1, which is not observed.

Figure 13 shows a model for the distribution of axial ratios that fits the observations for Im galaxies. The model calculates the distribution of projected b/a for random orientations of triaxial ellipses that have intrinsic ratios of width (W) to length (L) uniformly distributed in the range 0.7 to 1, and intrinsic ratios of thickness (Z) to length uniformly distributed in the range 0.29 - 0.67 (see discussion of triaxial models in Elmegreen et al. 2005). If this is the explanation for the distribution of apparent axial ratios in Im galaxies, then they are triaxial with an average ratio of around L:W:Z=1:0.85:0.48. This is similar to what Sung et al. (1998) found—L:W:Z=1:0.7:0.5 (see also Binggeli & Popescu 1995).

However, Figures 14 and 15 suggest the situation is slightly more complicated than this. Here we plot  $\mu_{2.5R_D}$ , integrated  $\mathcal{M}_{V_0}$ ,  $2.5\mathcal{R}_D^V$ , and  $(B-V)_0$ , all as functions of b/a. Here  $\mu_{2.5R_D}$  is the average V-band surface brightness within  $2.5\mathcal{R}_D^V$ , normalized to the area in the ellipse that integrates the light at  $2.5\mathcal{R}_D^V$ , rather than the circular area in the plane of the galaxy used for the values given in Table 5;  $\mu_{2.5R_D}$  is smaller (brighter) than  $\mu_{2.5D}$  listed in Table 5 by  $2.5\log{(a/b)}$ . The three galaxy types are plotted with different symbols and colors, and the lines are averages for each type in intervals of 0.1 in b/a.

The top part of Figure 14 indicates that the  $\mu_{2.5R_D}$  values for Im galaxies at the peak of the b/a distribution are clustered near the limit of detection, which is at the lower part of the panel. The two figures further show that the sizes and luminosities are smallest at the peak of the b/a distribution. Outside of these regions in the figures, the distribution of b/a values is more uniform. This suggests that the smallest and faintest Im galaxies could be triaxial, but the larger and brighter Ims are more disk-like.

An alternative possibility for this distribution is that we have observed only the edge-on examples of the Ims that have very low intrinsic surface brightness. An edge-on projection of a disk has a higher apparent surface brightness than the face-on projection, in proportion to the ratio of optical path lengths. Thus the extremely faint Im's could be visible only when viewed edge-on (see Elmegreen et al. 2005).

The bottom part of Figure 14 indicates that all galaxy types in our sample brighten slightly as b/a increases, and correlation coefficients are consistent with this. The increase follows from the near-constant values of surface brightness and size as a function of b/a for each type. Larger b/a then corresponds to larger projected area and more exposed galaxy. Such a correlation is expected to appear whether or not we select against the face-on versions of the lowest surface brightness galaxies. It would not appear if the galaxies were optically thin, but the largest increase is for the BCDs, which probably have the most opacity.

The bottom part of Figure 15 suggests that  $(B-V)_0$  for BCD galaxies reddens with increasing b/a. This color does not change noticeably for the other types. The origin of this

seems to follow from the radial distribution of colors for BCDs (see Figure 34 below) if the inner starburst parts of these galaxies are more spherical than the outer old red disk. Then the change from edge-on to face-on will brighten up the red outer disk but not brighten the inner blue starburst as much. The result is an overall redder color along with the total brightening for more face-on cases.

### 4.3. Colors

# 4.3.1. Integrated photometry

The integrated colors are shown in color-color plots: UBV in Figure 16, JHK in Figure 17, and VJH in Figure 18. The irregular galaxies are bluer in UBV than spirals, as is well known (de Vaucouleurs, de Vaucouleurs, & Buta 1983). There is, however, a large range—0.5 mag—in the UBV colors within the sample. In J—H, the colors fall between those of an H II region, which represents a very young stellar population, and those of a globular cluster, which represents a very old stellar population. The spirals that were observed for comparison lie near the globular cluster. The H–K colors of these objects are not well separated.

### 4.3.2. Gradients

Most Im galaxies are remarkably uniform in color, showing no change with radius (see, for example, Bergvall et al. 1999, van Zee 2000). However, this is not universally true of the class. In Makarova et al.'s (2002) study of 16 nearby dwarfs, about half showed some gradient, becoming redder in the outer parts. Similar results were found by Parodi, Barazza, & Binggeli (2002). Of the 94 Im galaxies in our sample, 44 (47%) show a radial gradient in at least one color. Surface photometry with a gradient that could be equally well fit with a constant color within the uncertainties is not counted. Also, a variation from a constant color of only 1–2 annuli was not counted as a gradient since these are probably due to individual star-forming complexes. Gradients are also seen in 13 of 24 BCDs (54%) and 14 of 18 (78%) of our Sms. For these galaxies, the color gradients are given in Table 6. The gradients, when present, however, tend to be small. The minimum gradients that we detected were 0.02 mag kpc<sup>-1</sup> in B–V and U–B, 0.04 mag kpc<sup>-1</sup> in J–H and H–K, and 0.09 mag kpc<sup>-1</sup> in V–J. The typical gradient, when present, in B–V is 0.1 mag kpc<sup>-1</sup> and in V–J is 0.3 mag kpc<sup>-1</sup>.

For comparison, de Jong (1996c) examined the BVRIK color gradients in 86 face-on spiral galaxies. All galaxies became bluer with radius, and all colors were strongly correlated. Gadotti (1999) has also examined color gradients in Sbc spirals. He found that 25% had

no gradients, but most of these are barred and he suggests that the stellar bar potential induces radial mass flows to the center, serving to homogenize the stellar population. Of the rest, 65% have gradients that become redder to the center and 10% become bluer to the center. Bell & de Jong (2000) and MacArthur et al.'s (2004) analysis of large samples of spiral galaxies showed "significant" color gradients in all of the galaxies with most being redder in the central parts.

One striking feature of those galaxies in our survey showing measurable gradients is the great variety in the profiles. Among the Im galaxies with color gradients, 67% (24 galaxies) with a gradient in B–V become redder with radius and 56% (20 galaxies) with a gradient in U–B become redder. By contrast most (10 of 15 gradients, 8 of 9 galaxies) become bluer with radius in J–H, H–K, or V–J. About 26% of the UBV profiles (in 15 galaxies) are complex, illustrated with NGC 2552 in Figure 19, becoming redder or bluer or staying flat at different radii within a galaxy. Among the BCDs with color gradients, 75% become redder with radius in B–V and 91% in U–B. All (6 gradients in 5 galaxies) become redder in the VJH colors as well. Of these systems with B–V gradients 42% have complex profiles, and one also has a complex U–B profile. Of the Sm systems, 87% of the color gradients in the UBVJH colors become bluer with radius. Six galaxies (40%, 8 gradients) have complex profiles. MacArthur et al. (2004) saw similar behavior among their spiral galaxy sample: The color gradients in the inner part and outer part sometimes had different slopes, and sometimes changed sign.

Bell & de Jong (2000) and MacArthur et al. (2004) have examined the relation between age gradients in spirals, derived from color gradients, and various galactic parameters. They find a correlation between age gradients when the radius is normalized to the disk scalelength and the luminosity and size of the galaxy. Bell and de Jong also find a correlation with the central surface brightness which MacArthur et al. do not see when the gradient is normalized to the scale-length of the disk. In Figure 20 we plot the B-V color gradient, normalized to  $R_D^V$ , against these three galactic parameters. The black symbols are the second parts of two-part gradients (see Table 6). Most of the Im galaxies, covering the entire range of observed  $M_V$ , have zero gradients. However, for those galaxies in our sample that do exhibit gradients, we see that the color gradient correlates with  $M_V$  only in the sense that the Sm galaxies are both systematically more luminous and also systematically have negative color gradients (redder in the central regions). Similarly, there is a correlation of color gradient with  $R_D^V$  only in the sense that the Sm systems extend to bigger systems compared to BCDs and Im galaxies and dominate the negative side of the plot. However, it is plausible that the spiral galaxies, which are more luminous and larger than our sample galaxies, would extend the Sm part of parameter space on our plots, placing our sample as part of the correlations seen by these researchers. Like, MacArthur et al. we see no correlation with  $\mu_0^V$ .

Another striking feature of some of the survey galaxies is that color gradients are not correlated among the different pass-bands as might be expected if different colors emphasize different stellar populations. An example of this is shown for NGC 2552 in Figure 19. In addition, three of the BCDs have B-V and U-B profiles with opposite gradients. We have not measured the JHK colors as far out in radius as the UBV colors, so we do not know what the JHK are doing in the outer parts, where one might see changes in the optical colors. However, among the galaxies with J, H, or K measurements in addition to UBV, at least one JHK color, including V-J, does not show the same sort of general trends or variations as the optical colors in 12 of the Im galaxies, while in another 14 the colors are correlated. Among the BCDs, 1 shows different passbands doing different things, and in 11 systems the colors track each other. Among the Sms, 2 galaxies show different trends in different colors and in 1 they follow the same trend. In most spiral galaxies, on the other hand, the colors are strongly correlated (de Jong 1996c). However the color-color diagrams in Bell & de Jong (2000) and MacArthur et al. (2004) show kinks in some of the radial profiles of spirals as well.

Color gradients are the result of a mixture of stellar age gradients, metallicity gradients, and extinction gradients. The generally blue centers of the BCDs are probably the result of recent star formation following some major inflow of gas (Hunter & Elmegreen 2004). The mixed color gradients in the other types may reflect a patchy history of star formation. Extinction gradients should cause all of the disk colors to vary in the same way with radius. Figure 21 shows B-V and V-J colors from Bruzual & Charlot (2003) models using the Padova1994 evolutionary tracks and the Chabrier (2003) stellar initial mass function (IMF). The five different curves are for different metallicities, as indicated by the colored lines. On the left are the galaxy colors for a single burst stellar population that has aged for the time indicated on the abscissa. On the right are models with star formation rates decaying exponentially, as  $\exp(-t/\text{decaytime})$ , starting 10 Gyr ago (at t=0) and continuing until today (at  $t = 10^{10}$  yr). When the decay time is small, the stars are all old and the colors resemble the single stellar population models for large ages. When the decay time is large, the models are like continuous star formation. Starburst models have colors indicated by the low age asymptote in the left-hand panels. The figure has the usual result that both increasing age and decreasing metallicity cause a population of stars to redden. However, there are cases where B-V can get redder while V-J gets bluer, as observed for 3 of our Im galaxies. This may happen, for example, when the inner region has a dominant age of  $\sim 10^7$ yr and a moderately high metallicity (e.g. Z = 0.008) while the outer region has a dominant age of  $10^8 - 10^9$  yr and a lower metallicity. Thus, the changes in color gradients within a galaxy probably reflect the large-scale bubbling of star formation activity around the galaxy over time, and the uncorrelated behavior of colors reflects how recently star formation has occurred in a given annulus.

### 4.3.3. Two-dimensional color-color images

Azimuthally-averaged color profiles are not always an adequate indicator of color structure in the galaxy. For example, color profiles are uniform with radius in NGC 2366 and NGC 4449. Yet, Hunter et al. (1999, 2001a) found that both of these barred systems have a bright, blue ridge that crosses from one corner of the rectangular inner bar to the opposite corner. Figure 22 illustrates this with color-ratio images. These are the only two Im galaxies that we have found that show this kind of color structure, but they do provide a caution that motivated us to carefully examine two-dimensional color-color ratio maps of each galaxy in our sample. (All of the color ratio images are available from http://www.lowell.edu/users/dah/colormaps/).

For most of our galaxies the two-dimensional color ratio images look as expected: The azimuthally-averaged colors are flat with radius and the two-dimensional ratio images are uniform. The optical UBV ratio images are punctuated with blue spots that correspond to H II regions while the JHK ratio images do not show structure.

Some variations from this picture are the natural consequence of variations in the evolutionary status of individual star-forming regions. In some galaxies, especially the BCDs, some H II regions are associated with red knots in B/V or U/B (A1004+10, DDO 27, F533-1, Haro 4, Haro 8, Haro 20, Haro 29, Haro 38, VIIZw 403). Presumably the red knots are dominated by red supergiants, evolved massive stars. There are also blue knots (DDO 50, DDO 120, DDO 167, DDO 187, DDO 216, F564-V3, M81dwA, NGC 1569, NGC 2552, NGC 3413, NGC 3738, WLM) and red knots (CVnIdwA, DDO 25, DDO 215, F721-V2, Mrk 178, NGC 4214) that do not correspond to H II regions, and these probably represent regions that are old enough for the H II region to have dissipated. Interestingly, there are also blue rings with red holes (DDO 33, DDO 155, Haro 3, Mrk 5, Mrk 408) that are sometimes associated with an H $\alpha$  hole or ring of H II regions (Mrk 16, Mrk 757, VIIZw 403). These are probably instances of star-induced star formation, with the blue ring representing the second generation.

On a larger scale, others have noted that some irregular galaxies have extended red stellar populations while the blue stars are more concentrated to the center of the galaxy (WLM: Minniti & Zijlstra 1996; DDO 210: Lee et al. 1999; NGC 3109: Minniti, Zijlstra, & Alonso 1999; DDO 190: Aparicio & Tikhonov 2000; DDO 187: Aparicio, Tikhonov, & Karachentsev 2000; Makarova et al. 2002; Hidalgo, Marín-Franch, & Aparicio 2003b). This

is especially true of BCDs in which the current star formation is often intense and centrally located (Kunth 1987; Papaderos et al. 1996; Thuan, Izotov, & Foltz 1999; Cairós et al. 2003; Noeske et al. 2003).

In our sample, we also see that some of the galaxies have blue centers and relatively red ( $\Delta(B-V)\sim0.5$ ) or somewhat redder ( $\Delta(B-V)\sim0.1$ –0.2) outer parts. In the cases of A1004+10, DDO 70, DDO 120, DDO 168, DDO 216, F565-V1, Haro 23, Haro 38, Mrk 32, Mrk 408, Mrk 757, NGC 1569, NGC 3738, NGC 3952, NGC 4163, NGC 6789, WLM, and VIIZw 403, this color structure is clear in the azimuthally-averaged surface photometry. But, for Haro 36 and NGC 3413 the surface photometry does not show this because the blue structures are elongated along the major axis. However, other galaxies have relatively red ( $\Delta(B-V)\sim0.1$ –0.3) centers and bluer outer parts (DDO 9, DDO 24, DDO 48, DDO 50, DDO 88, DDO 105, DDO 122, DDO 173, DDO 180, DDO 204, DDO 214, F563-V2, F651-2, NGC 2552, NGC 3510, UGC 5716).

Some galaxies show large-scale blue or red regions that are not aligned with the center and some of these regions occupy nearly half of the galaxy (DDO 155, DDO 165, DDO 171, Haro 3, UGC 5209). This was also seen for the BCD Tol 3 by Noeske et al. (2003). Sometimes the H II regions are not located in the part of the galaxy that is blue in B–V (F620-V3, Haro 14, HS 0822+3542). The large-scale patchiness in colors most likely indicates bulk variations in the stellar populations, and are clear indications of the manner in which star formation can bubble around the galaxy on scales of kiloparsecs (Hunter & Gallagher 1986).

DDO 165 and NGC 3413 merit a special note for their peculiar color structure. DDO 165 has a very sharp, curved southern edge and this edge is bluer than the rest of the galaxy. NGC 3413 has a narrow, high surface brightness blue ridge down the middle of a redder, broader disk. The blue ridge extends the length of the galaxy, but H II regions are found only in the center.

Galaxies with some type of peculiar color structure are flagged in Table 5. Of the Im group 23 (24%) have some peculiar color structure, while 11 (46%) of the BCDs and 10 (56%) of the Sms do.

### 4.3.4. Relationship between colors and gas surface density

We have examined the relationship between changes in the azimuthally-averaged color profiles and variations in the gas surface density. The motivation here is that the gas is the fuel for star formation, and one might expect that regions with a greater reservoir of fuel would more readily form stars and that this would be reflected in the bulk stellar populations as revealed in the optical colors. The H<sub>I</sub> profiles that are available in the literature for galaxies in our survey are shown in the figure discussed in §4.4.3 and the references are given in that figure caption.

We consider the ratio of the observed gas surface density  $\Sigma_q$  to the critical gas density  $\Sigma_c$ derived from the gravitational instability models for differentially-rotating disks (Safronov 1960, Toomre 1964, Quirk 1972). In these models there is a critical column density  $\Sigma_c$  above which the disk is unstable to ringlike perturbations and can easily form star-forming clouds, and below which the disk is stable and less likely to form clouds. The rotating gas disk model was applied by Kennicutt (1989) to spiral galaxies to explain the apparent drop off in star formation in the outer regions (see more detailed models of this drop-off in Elmegreen & Hunter 2005). Hunter & Plummer (1996), Meurer et al. (1996), van Zee et al. (1997a), and Hunter, Elmegreen, & Baker (1998) have applied this model to Im galaxies and found that it fails to predict where star formation occurs in Im galaxies. However, we now take a fresh look at the relative  $\Sigma_g/\Sigma_c$  in the context of color profiles within galaxies. We use the  $\Sigma_c$  and  $\Sigma_q/\Sigma_c$  derived by Hunter, Elmegreen, & Baker (1998) for 12 of the galaxies in our survey.  $\Sigma_c = Ac\kappa/\pi G$ , where  $\kappa$  is the epicyclic frequency, c is the velocity dispersion of the gas, and A is a constant determined by Kennicutt to be of order 0.7. The  $\kappa$  were derived from the H<sub>I</sub> rotation curves whose references are given in our earlier study. There were observed velocity dispersions available for 4 galaxies in the range from 6.8 to 9.5 km  $s^{-1}$ ; the rest were assumed to be 9 km  $s^{-1}$ .

We find no clear connection between  $\Sigma_g/\Sigma_c$  and azimuthally-averaged colors. In IC 1613 the outer part of the galaxy does begin to become redder in B–V and U–B just where  $\Sigma_g/\Sigma_c$  and  $\Sigma_{H\alpha}$  begin to drop in value. A lower value of  $\Sigma_g/\Sigma_c$  should mean that it is harder to form stars, and hence the redder stellar population would be consistent with this. On the other hand, in DDO 155 there is a small gradient to redder colors in the outer parts where there is a gentle trend to  $higher \Sigma_g/\Sigma_c$ . In NGC 2366 and DDO 154, the colors and  $\Sigma_g/\Sigma_c$  are fairly constant with radius. On the other hand, in DDO 50 there is a large abrupt change in  $\Sigma_g/\Sigma_c$  at a radius of 2.75' accompanied by only a minor, smooth trend in B–V and constant U–B. Similarly, there is a rather large change in  $\Sigma_g/\Sigma_c$  in DDO 105, DDO 168, and F563-V2 where there is only a very small (<0.2 mag) change in colors.

We also examined the possibility of a correlation between the colors and the simple gas column density  $\Sigma_g$ , but again we do not see a consistent pattern. However,  $\Sigma_g$  is relatively flat within the confines of the optical galaxy in 8 of 9 galaxies (see §4.4.3 and the figure discussed there); in these systems  $\Sigma_g$  drops by a factor of 1.5—3.8 over the region that colors are measured. DDO 168 is the exception in that  $\Sigma_g$  drops by a factor of 9.8 over the radius of the optical galaxy, but the optical colors are, nevertheless, relatively constant with radius.

### 4.4. Exponential disks

### 4.4.1. Disk scale-lengths and surface brightnesses

Hodge (1971) pointed out that Im galaxies possess exponential disks, and all of the surface brightness profiles of the galaxies in our sample are well fit, at least in part, with an exponential. Histograms showing the number distributions of the V-band scale length  $R_D^V$  and central surface brightness  $\mu_0^V$  from the fits to surface brightness profiles are shown in Figures 23 and 24 (see also van der Kruit 1987). Figure 23 can be compared to Figure 15 of Swaters & Balcells (2002) which presents R-band disk scale-lengths for a large sample of Im galaxies. The two distributions are similar. The median values of  $R_D^V$  and other disk parameters for our sample are given in Table 7. Similar values for the J-band fit are also given in Table 7, and a comparison of V-band and J-band  $R_D$  is shown in Figure 25. For most galaxies the disk scale-length measured at J is close to that measured at V (see also Bergvall et al. 1999; Doublier et al. 2001; Cairós et al. 2003; Noeske et al. 2003), implying that the older stars and younger stars trace the same disk structure.

Papaderos et al. (1996) observed that the underlying disks in BCDs have smaller  $R_D$  by a factor of two compared to Im galaxies of the same luminosity. Patterson & Thuan (1996) found that the dIms divide into two groups: one group has twice the scale-length of BCDs at the same luminosity and the other group has the same scale-length. A plot of  $R_D^V$  as a function of  $M_{V_0}$  for our sample is shown in Figure 26. We see a separation of the Im and BCD galaxies, with the BCDs having shorter scale-lengths. The Sm galaxies fall between the Im galaxies and BCDs in scale-length at a given galactic absolute magnitude. We also see a strong correlation between  $M_V$  and  $R_D^V$ , first pointed out by Hodge (1971) and seen in spirals (for example, MacArthur et al. 2004), in which lower luminosity galaxies have smaller scale-lengths. We also see a separation of systems in central surface brightness  $\mu_0^V$ , shown in the right panel of Figure 26, as expected: BCDs are small and high surface brightness, Ims are lower in surface brightness and come in a range of sizes, and Sms tend to be larger systems that are in between BCDs and Ims in surface brightness.

### 4.4.2. Comparison with spirals

The exponential disks of a large sample of spirals have been examined by de Jong (1996b), and it is useful to see how our sample of galaxies compares to that sample. In de Jong's Figure 3, reproduced here for V-band as the top panel of Figure 27, we see that the average  $\mu_0^V$  of the spiral galaxies increases slightly with later galactic Hubble type, with a scatter typically of 1–2 mag in 1 arcsec<sup>2</sup> (see also Roberts & Haynes 1994). The median

values from the Sm, Im, and BCD samples is shown as the horizontal line for the last 3 galaxy types in Figure 27. The median central surface brightnesses of our Sm and Im samples continue the general trend seen in the spiral galaxies by de Jong although the range of  $\mu_0^V$  for the Im galaxies is over 6 magnitudes. The BCD central surface brightnesses, however, are considerably larger, 2.1 mag brighter on average than the Im sample, and these systems stand out as unusually bright.

De Jong's (1996) Figure 4, reproduced here for V-band as the bottom panel of Figure 27, shows the disk scale-lengths  $R_D^V$  (see also Freeman 1970, Roberts & Haynes 1994). Again, the scatter is large for a given galaxy type, and there is no obvious trend with galactic Hubble type for the spirals. The Im, BCD, and Sm samples all have median scale-lengths that are smaller than those of the spirals, and BCDs are smaller than the Ims which in turn are smaller than the Sms. But again, the range is quite large within each type.

De Jong's (1996) Figure 5 shows a plot of scale-length versus central surface brightness, reproduced here for V-band as the right panel of Figure 26. Our systems lie to the lower left in this figure with smaller scale-length and fainter central surface brightness. As de Jong points out, there is not much of a trend, and our irregular galaxies just increase the scatter. The left panel of Figure 26, discussed in the previous section, shows  $R_D^V$  plotted as a function of galactic  $M_V$  with de Jong's spirals. The spirals and Im/BCD/Sm galaxies produce a strong correlation (see also Freeman 1970). Such a correlation is also seen for a very large sample of luminous disk galaxies observed with the Sloan Digital Sky Survey (SDSS; Blanton et al. 2003).

Figure 28 shows the distribution of extrapolated central surface brightness  $\mu_0^V$  versus galaxy magnitude  $M_{V_0}$  for all of the primary exponential disks in our survey. The dashed line is the average Freeman (1970) value for spiral galaxies (see also Phillipps et al. 1987; van der Kruit 1987, 1989). Freeman's  $\mu_0^B = 21.65$  mag arcsec<sup>-2</sup> has been corrected for reddening in the same fashion that the spirals on this plot have been corrected (E(B-V)<sub>i</sub> = 0.3) and a (B-V)<sub>0</sub> = 0.6 is used to convert  $\mu_0^B$  to  $\mu_0^V$ . There is a lot of scatter, but overall the fainter galaxies have fainter central surface brightnesses than the brighter galaxies (see also de Jong & van der Kruit 1994, Roberts & Haynes 1994, Burstein et al. 1997). On average they approach the Freeman value at around  $M_{V_0} \sim -19$ . The BCDs have the highest  $\mu_0^V$  and the Im types have the lowest in our sample, as mentioned previously (see Fig. 24). A correlation between luminosity and central surface brightness is also seen for luminous disk galaxies observed with SDSS (Blanton et al. 2003). From the slope of the correlation they conclude that the median size of galaxies increases with luminosity, especially for the most luminous galaxies.

# 4.4.3. Complex surface brightness profiles

While most of the sample galaxies have a V-band surface brightness profile that is well fitted with a single exponential disk, there are others that have more complex profiles. The four types of variations that we see are shown in Figures 29 to 34. Each galaxy is offset vertically for clarity; the major ticmarks on the ordinate correspond to 2 mag arcsec<sup>-2</sup>. The bottom panels in each figure show B–V color profiles, with large ticmarks corresponding to 0.2 mag and red increasing toward the top.

Of the Im galaxies, 23 (24%) have one of these complex types of profiles along with 10 (42%) BCDs and 8 (44%) Sms. The most common two-part profile (20 galaxies) is one in which the light in the outer part of the galaxy drops more steeply (Figures 29 and 30). This was seen in two Im galaxies by Hidalgo et al. (2003b), one of which is also in our sample. This type of behavior has also been seen in the outer parts of spirals (van der Kruit & Shostak 1982; Shostak & Van der Kruit 1984; de Grijs et al. 2001; Kregel et al. 2002; Pohlen et al. 2002; Kregel & van der Kruit 2004), including one low luminosity spiral (Simon et al. 2003). (See also some of the surface brightness profiles of spirals shown by Bell et al. 2000 and MacArthur et al. 2003). It is now also seen in disks at high redshifts (0.6 < z < 1.0; Pérez 2004).

Ten galaxies show a profile that is approximately flat over a significant part of the galaxy, and these galaxies are plotted in Figures 31 and 32. This was also seen for M81dwA and UGC 3817 by Patterson & Thuan (1996). DDO 68 is the only case in our sample where the profile is nearly flat in the outer regions, but this feature was also seen in the BCDs Tol 1214–277 and Tol 65 by Noeske et al. (2003) and Cam 1148–2020 by Telles, Melnick, & Terlevich (1997).

Figures 33 and 34 show profiles in which the light in the outer part of the galaxy drops off less steeply compared to the inner regions. This is seen in 11 galaxies: 8 BCDs, two Im galaxies with BCD-like characteristics (IC 10 and NGC 3738), and one normal Im (DDO 40). This type of behavior is expected in BCDs and other galaxies where the centrally concentrated star formation or starburst steepens the surface brightness profile there (Papaderos et al. 1996; Cairós et al. 2001; Noeske et al. 2003). The corresponding decrease in B–V for young stars in the central steep part is seen in Figure 34. Unlike Doublier et al. (1999), we do not find BCDs that are better fit with an r<sup>1/4</sup> law, although the average curvature in such a law, on a surface-brightness versus radius plot, is the same as on our double-exponential profiles where the outer part is relatively flat.

The division between the sub-sample with "steep outer profiles" and that with "flat inner profiles" is somewhat arbitrary. There are those galaxies, such as DDO 75, DDO

168, DDO 185, M81dwA, and UGC 8011, with no surface brightness gradient in the central regions. Then there are those, such as DDO 69, Mrk 178, and UGCA 290, that have a short but noticeable central gradient. Finally, F651-2 has a shallow, but more prolonged, gradient in the center. It is arguable whether this last galaxy, in particular, belongs in the "flat inner profile" group or the "steep outer profile" group. However, in our modelling of these profiles (Elmegreen & Hunter 2005), we combine these two groups together, and so the exact line between them is not so important.

Figures 29 to 31 show most of the double exponential profiles that get steeper with radius. The profiles are all qualitatively the same, although those in Figure 31 are flatter in the inner regions. The Sm galaxy colors tend to get bluer with radius at first and then level off, while the Im galaxy colors are a little more constant near the center and then get redder with distance. These B–V color variations most likely reflect variations in the mean stellar population ages and, possibly, metallicities, with a small dependence on extinction (§4.3.2).

Statistics on where the break in the V-band profile  $R_{Br}$  occurs relative to  $R_H$ ,  $R_{1/2}^V$ , and  $R_D^V$  are given in Table 8. The  $R_D^V$  used in this ratio is the scale-length of the main disk: the inner exponential for the profile that steepens in the outer parts and the outer exponential for the profile that is shallower in the outer parts. We see that the average location of the profile break relative to the Holmberg radius is similar whether the profile steepens or becomes shallower in the outer parts. However, a flat profile covers a somewhat smaller fraction of the galaxy.

Relative to the disk scale-length, the break in the profile of Im galaxies occurs on average at a radius of 1.5–1.7 scale-lengths while that in the BCDs occurs on average at 1.9–2.2 scale-lengths. This is shown in Figure 35. Galaxies with brighter central surface intensities tend to have larger ratios  $R_{Br}/R_D^V$ , as noted by Pohlen et al. (2004) and Kregel & van der Kruit (2004) for spirals. The break in the profiles of Pohlen et al.'s (2002) three spirals occurs further out at 3.9±0.7 scale-lengths. Van der Kruit & Shostak (1982) and Shostak & van der Kruit (1984) also found longer break radii—4.2 and 3.1 scale-lengths—for two spirals, and Kregel & van der Kruit (2004) found break radii (which they called truncation radii) at ~4 scale-lengths for a large group of high surface brightness spirals. However, de Grijs et al.'s (2001) four spirals have breaks ranging from 1.6 to 3.3 scale-lengths, similar to the irregulars observed here. The disks measured at high redshift show breaks at about 1.8 scale-lengths (Pérez 2004), more like the Im galaxies than local spirals.

In Table 8 we also present the ratio of the inner scale-length  $R_{D,i}$  to outer scale-length  $R_{D,o}$  in V-band for the two-part exponentials. In Pohlen et al.'s spirals this ratio is  $2.0\pm0.2$  which is similar to the ratio for our Im and Sm galaxies with the steepening exponential disk. Van der Kruit and Shostak's ratios bracket Pohlen's ratio with values of 1.6 and 2.6.

What causes this break in the surface brightness profile? We compared the locations of the break to the H $\alpha$  surface brightness profiles in order to see what was happening with the star formation activity at that radius. We see that, of the 40 galaxies with complex profiles, in 15 most of the detectable H $\alpha$  ends within one annulus of the location of the break. In another 18 galaxies, the H $\alpha$  surface photometry drops more rapidly beginning approximately around R<sub>Br</sub>. Thus, in 83% of these galaxies there is some change in  $\Sigma_{H\alpha}$ , and this would be a satisfying explanation to the change in stellar surface brightness. However, in 7 of the galaxies the H $\alpha$  profile does not change or H $\alpha$  ends well before the break. Furthermore, there are 30 Ims (32%), 11 (46%) BCDs, and 1 (6%) Sm that also exhibit a change in the drop off rate of  $\Sigma_{H\alpha}$  or H $\alpha$  ends well before  $\mu_{V_0}$ , and yet they do not show a break in their V-band surface brightness profiles. Pohlen et al. (2002) also could not find a convincing correlation with H $\alpha$  in spirals.

 ${\rm H}\alpha$  is a measure of the current star formation, whereas the broad-band colors integrate the star formation over longer periods of time. Therefore, one might expect a better correlation between the breaks in the surface brightness profiles and changes in color profiles. Among those galaxies with nearly flat inner profiles 5 of 10 show a change in B–V where the break in  $\mu_{V_0}$  occurs. All of these become redder beyond the break. Of those with an exponential that becomes steeper, 7 become redder after the break, 1 becomes bluer, and 11 do not change. The galaxy with the flat outer profile shows no change in color with radius.

We have also compared the broad-band and H $\alpha$  surface photometry to the surface density of the neutral gas  $\Sigma_{HI}$ . We plot  $\mu_{V_0}$ ,  $\Sigma_{H\alpha}$ , and  $\Sigma_{HI}$  in Figure 36 for all survey galaxies with H I surface density profiles  $\Sigma_{HI}$  available from the literature (see the references listed in the figure caption). This includes three galaxies with breaks in their exponential profiles (DDO 75, DDO 105, and DDO 168) and 9 that have single exponential profiles. One can see that azimuthally-averaged  $\Sigma_{HI}$  has very little correspondence with what is going on in the optical, including the breaks in the exponential profiles, as well as changes in UBVJHK colors (not shown in the figure but discussed in §4.3.3). Generally,  $\Sigma_{HI}$  changes very slowly over the optical galaxy, and when the change is more rapid, there is no correspondence with optical changes.

Similarly, there is no correlation between where the break in the surface brightness profile occurs and changes in the H<sub>I</sub> rotation curve of the galaxy (from the references in the caption to Figure 36 and Swaters 1999). The break occurs after the rotation curve turns over in 5 galaxies, during the solid body part of the rotation curve in 4 galaxies, and about at the turn over in the rotation curve in 1 galaxy. Five galaxies show no measurable rotation.

In a separate paper (Elmegreen & Hunter 2005) we present a model of star formation in outer galaxy disks that reproduces the observed double exponential profile and the correlation

between break radius and galaxy magnitude. The model is based on the concept that both gravitational instabilities and compression trigger star formation, and that in the outer disk, beyond the Kennicutt (1989) surface density threshold, only the compression from low level turbulence and sporadic supernovae remain. Because of this, the star formation rate in the outer disk does not drop suddenly at the threshold, but has a more gradual, exponential-like decline.

# 5. On the Dalcanton et al. (2004) study of Dust Lane Thickness

Dalcanton et al. (2004) proposed that large spiral galaxies have thin dust and gas layers and small irregulars have thick dust and gas layers or no obvious dust layers because the large galaxies are more gravitationally unstable and this enhanced instability makes the gaseous velocity dispersions in those galaxies smaller. While it may be that spirals are more unstable than irregulars ( $\S1$ ), this is probably not the explanation for the difference in gas layer thickness. As recognized by Dalcanton et al., thickness depends only on the velocity dispersion and gravitational acceleration perpendicular to the plane, while stability depends on the epicyclic frequency as well. Thus thin gas layers can be in either stable or unstable disks, as can thick gas layers, depending on the ratio of the perpendicular crossing time (which is the thickness divided by the velocity dispersion) to the epicyclic time. This ratio is the Toomre stability parameter Q.

Figure 6 suggests that the reason for the Dalcanton et al. (2004) correlation between gas layer thickness and galaxy type is that normal spirals have  $\sim 10$  times higher surface densities than irregular galaxies, corresponding to a difference in surface brightness of 2.8 magnitudes in 1 arcsec<sup>-2</sup>. In contrast, the velocity dispersions of the gas (c) do not vary much among these different types, regardless of stability. Thus, the gaseous scale height, which is proportional to  $c/(\pi G\Sigma)$ , is high in irregulars because the surface density is low. This is related to our previous observation that the general interstellar medium pressure is lower in irregulars than in spirals (Elmegreen & Hunter 2000): the larger scale height makes the average space density lower and the pressure lower for a given gas column density and velocity dispersion.

In a disk composed of both gas and stars with small ratios of the gaseous to stellar  $(c_s)$  velocity dispersions and masses, the gravitational acceleration perpendicular to the plane is determined mostly by stars and it increases linearly with height z approximately as  $g(z) = zg_0/H_s$  for constant  $g_0$  (this is an approximation to the  $\tanh(z/H_s)$  distribution of an isothermal stellar disk of scale height  $H_s$ ). The scale height H for the gas is then given by  $c^2/H \sim g(H)$ , which reduces to the relation  $H = c (H_s/g_0)^{1/2}$ . It follows that an

approximate relation between the stellar and gaseous scale heights and velocity dispersions is  $H/H_s \sim c/c_s$ . If the gaseous dispersion is somewhat uniform between galaxy types, and the stellar dispersion is higher in large spirals (Dalcanton et al. 2004), then the ratio of the gaseous to the stellar scale heights is smaller in spirals than in irregulars, making the dust lanes look much thinner in spirals compared to the background stellar disk. The absolute gaseous scale height is also larger in irregulars because the stellar disk thickness is larger (§4.2.3). All of these differences are unrelated to the degree of disk stability.

Another reason dwarf galaxies have imperceptible dust lanes is that the metallicity is low, making the extinction low per unit gas column density, and the line of sight depth is low because of the small galaxy size. Thus, the total opacity to dust is much lower in edge-on dwarfs than in edge-on spirals. An exception may be for the starburst cores of BCDs, which could have a significant opacity because of the high average gas density.

These points suggests that the Dalcanton et al. (2004) correlation between dust lane thickness and galaxy rotation speed may be explained in general terms by variations in the stellar surface density and line-of-sight opacity. There is no obvious reason for the reported suddenness of the transition at a rotation speed of 120 km s<sup>-1</sup>, but it could be from the combination of these two effects. That is, the interstellar medium for an edge-on galaxy could become nearly optically thin between the center and the edge at about the same rotation speed as the average stellar surface density starts to drop by a factor of 10. For example, this drop occurs in Figure 28 at about  $M_{V_0} \sim -19$  mag, and this corresponds to a rotation curve speed of  $\sim 120$  km s<sup>-1</sup> from Figure 1 in Hunter, Hunsberger, & Roye (2000).

#### 6. Conclusions

Observations of 136 Im, BCD, and Sm galaxies have been compiled to provide a large sample for statistical studies of galaxy colors, disk structures, and star formation processes in the most abundant types of galaxies in the Universe. The main results are:

- 1. The average and central surface brightnesses of Im galaxies are generally lower than in spiral galaxies by a factor of  $\sim 6$  ( $\sim 2$  mag in 1 arcsec<sup>2</sup>). The extrapolated central surface brightness for the main exponential part of the disk begins to drop below the standard Freeman value for spirals at  $M_{V_0}$  fainter than  $\sim -19$  mag. The low surface brightness of Im galaxies makes their disks and dust lanes thicker than in spirals, as observed by Dalcanton et al. (2004).
  - 2. Overall, Im galaxies are bluer than spirals. However, they show a wide range of colors,

complex color gradients, and complex color patterns, indicating an irregular mixture of stellar population ages, extinctions, and possibly metallicity gradients. Large-scale variations in colors are clear indications of the manner in which star formation can bubble around the galaxy on scales of kiloparsecs.

- 3. A normal fraction of Im galaxies are barred (23% of our Ims, 12% of our BCDs, and 50% or our Sms), but these bars tend to be larger than in spirals, relative to the disk scale length, sometimes occupying the entire bright part of the disk. The bars are also clearly associated with an excess of star formation in the Im galaxies. The bars are not often offset from the center of the galaxy.
- 4. In spite of a bias against obviously interacting systems in our sample, approximately one-third of the Im systems show large-scale morphological peculiarities that may be an indication of past interactions.
- 5. The radial profiles of surface brightness are usually well represented by an exponential over a large fraction of the disk, but many galaxies show two exponentials or other complex patterns. Some have flat profiles in the inner regions and a single exponential beyond that, others have two exponentials with either the inner one shallower or the inner one steeper. The cases with steeper inner exponentials also have significant blue excesses there, indicative of recently enhanced star formation in the centers. The cases with shallow inner exponentials show no obvious indications of their origin in peculiar star formation patterns, color gradients, H<sub>I</sub> profiles, or rotation curve features. Star formation models that combine gravitational instabilities with turbulence compression reproduce these profile features (Elmegreen & Hunter 2005).

We are deeply grateful to Ralph Nye who kept the Lowell Observatory Hall 1.1 m and Perkins 1.8 m Telescopes and their instruments operating and in excellent condition. We are also very thankful to Phil Massey for obtaining some of the UBV images for us and for doing the basic reductions of the Mosaic Imager images that he obtained. We wish to thank Emily Bowsher for geometrically matching some of the galaxies as part of the 2003 Research Experiences for Undergraduates program of Northern Arizona University funded by the National Science Foundation through grant 9988007. We also thank R. Shuping for obtaining several images as part of KPNO Service Observing. Funding for this work was provided by the Lowell Research Fund and by the National Science Foundation through grants AST-0204922 to DAH and AST-0205097 to BGE. This research has made use of the NASA/IPAC Extragalactic Database (NED) which is operated by the Jet Propulsion Laboratory, California Institute of Technology, under contract with the National Aeronautics and Space Administration.

Facilities: Lowell Observatory KPNO CTIO

### REFERENCES

Allsopp, N. J. 1978, MNRAS, 184, 397

Aparicio, A. 1994, ApJ, 437, L27

Aparicio, A., Gallart, C., & Bertelli, G 1997a, AJ, 114, 669

Aparicio, A., Gallart, C., & Bertelli, G 1997b, AJ, 114, 680

Aparicio, A., & Tikhonov, N. 2000, AJ, 119, 2183

Aparicio, A., Tikhonov, N., & Karachentsev, I. 2000, AJ, 119, 177

Barazza, F. D., Binggeli, B., Prugniel, P. 2001, A&A, 373, 12

Bell, E. F., Barnaby, D., Bower, R. G. de Jong, R. S., Harper, D. A., Jr., Hereld, M., Loewenstein, R. F., & Rauscher, B. J. 2000a, MNRAS, 312, 470

Bell, E. F., & de Jong, R. S. 2000, MNRAS, 312, 497

Bergvall, N., Rönnback, J., Masegosa, J., & Östlin, G. 1999, A&A, 341, 697

Binggeli, B., & Popescu, C. C. 1995, A&A, 298, 63

Blanton, M. R., et al. 2003, ApJ, 594, 186

Bottinelli, L., Gouguenheim, L., Fouqué, P., & Paturel, G. 1990, A&AS, 82, 391

Bremnes, T., Binggeli, B., & Prugniel, P. 1998, A&AS, 129, 313

Bremnes, T., Binggeli, B., & Prugniel, P. 1999, A&AS, 137, 337

Bremnes, T., Binggeli, B., & Prugniel, P. 2000, A&AS, 141, 211

Broeils, A. 1992, Ph.D. thesis, Rijksuniversiteit Groningen

Bruzual, G. & Charlot, S. 2003, MNRAS, 344, 1000

Bureau, M., & Carignan, C. 2002, AJ, 123, 1316

Burstein, D., Bender, R., Faber, S. M., & Nolthenius, R. 1997, AJ, 114, 1365

Burstein, D., & Heiles, C. 1984, ApJS, 54, 33

Cairós, L. M., Vílchez, J. M., González, Pérez, J. N., Iglesias-Páramo, J., Caon, N. 2001, ApJS, 133, 321

- Cairós, L. M., Caon, N., Papaderos, P., Noeske, K., Vílchez, J. M., Lorenzo, B. G., & Muñoz-Tuñón, C. 2003, ApJ, 593, 312
- Cardelli, J. A., Clayton, G. C., & Mathis, J. S. 1989, ApJ, 345, 245
- Carignan, C., & Beaulieu, S. 1989, ApJ, 347, 760
- Carignan, C., Beaulieu, S., & Freeman, K. C. 1990, AJ, 99, 178
- Carignan, C., & Freeman, K. C. 1988, ApJ, 332, L33
- Chabrier, G. 2003, PASP, 115, 763
- de Blok, W. J. G., McGaugh, S. S., & van der Hulst, J. M. 1996, MNRAS, 283, 18
- de Blok, W. J. G., & Walter, F. 2000, ApJ, 537, L95
- de Grijs, R., Kregel, M., & Wesson, K. H. 2001, MNRAS, 324, 1074
- de Jong, R. S. 1996a, A&AS, 118, 557
- de Jong, R. S. 1996b, A&A, 313, 45
- de Jong, R. S. 1996c, A&A, 313, 377
- de Jong, R. S., & van der Kruit, P. C. 1994, A&AS, 106, 451
- de Vaucouleurs, G. 1954, Observatory, 74, 23
- de Vaucouleurs, G. 1959, Handbuch der Physik, 53, 275
- de Vaucouleurs, G. 1963, ApJS, 8, 31
- de Vaucouleurs, G., de Vaucouleurs, A. 1972, MemRAS, 77, 1
- de Vaucouleurs, G., de Vaucouleurs, A., & Buta, R. 1983, AJ, 88, 764
- de Vaucouleurs, G., de Vaucouleurs, A., & Corwin, H. 1976, Second Reference Catalogue of Bright Galaxies (Austin, University of Texas Press), =RC2
- de Vaucouleurs, G., de Vaucouleurs, A., Corwin, H., Buta, R., Paturel, G., & Fouqué, P. 1991, Third Reference Catalogue of Bright Galaxies (New York, Springer-Verlag), =RC3
- Dickey, J.M., McClure-Griffiths, N.M., Stanimirovic, S., Gaensler, B.M, & Green, A.J, 2001, ApJ, 561, 264

Dohm-Palmer, R. C., et al. 1997, AJ, 114, 2527

Dohm-Palmer, R. C., et al. 1998, AJ, 116, 1227

Dolphin, A. E. 2000, ApJ, 531, 804

Dolphin, A. E., et al. 2002, AJ, 123, 3154

Dolphin, A. E., et al. 2003, AJ, 125, 1261

Doublier, V., Caulet, A., & Comte, G. 1999, A&AS, 138, 213

Doublier, V., Caulet, A., & Comte, G. 2001, A&A, 367, 33

Elmegreen, B.G. & Elmegreen, D.M. 1985, ApJ, 288, 438

Elmegreen, B.G., Elmegreen, D.M., & Leitner, S.N. 2003a, ApJ, 590, 271

Elmegreen, B. G., & Hunter, D. A. 2000, ApJ, 540, 814

Elmegreen, B. G., & Hunter, D. A. 2005, ApJ, submitted

Elmegreen, B.G., Kim, S., & Staveley-Smith, L. 2001, ApJ, 548, 749

Elmegreen, B.G., Leitner, S.N., Elmegreen, D.M., & Cuillandre, J.-C. 2003b, ApJ, 593, 333

Elmegreen, B.G., & Parravano, A. 1994, ApJ, 435, L121

Elmegreen, B.G., & Scalo, J. 2004, ARA&A, 42, 211

Elmegreen, D. M., & Elmegreen, B. G. 1980, AJ, 85, 1325

Ferguson, A. M. N., Wyse, R. F. G., Gallagher, J. S., & Hunter, D. A. 1998, AJ, 111, 2265

Ferraro, F. R., Pecci, F. F., Tosi, M., & Buonanno, R. 1989, MNRAS, 241, 433

Fioc, M., & Rocca-Volmerange, B. 1999, A&A, 351, 869

Fisher, J. R., & Tully, R. B. 1981, ApJS, 47, 139

Freedman, W. L. et al. 2001, ApJ, 553, 47

Freeman, K.C. 1970, ApJ, 160, 811

Gadotti, D. A. 1999, MSc. thesis, University of Sao Paulo

Gallagher, J. S., Hunter, D. A., & Tutukov, A. V. 1984, ApJ, 284, 544

Gallagher, J. S., Tolstoy, E., Dohm-Palmer, R. C., Skillman, E. D., Cole, A. A., Hoessel, J. G., Saha, A., & Mateo, M. 1998, AJ, 115, 1869

Gallart, C., Aparicio, A., Bertelli, G., & Chiosi, C. 1996a, AJ, 112, 1950

Gallart, C., Aparicio, A., Bertelli, G., & Chiosi, C. 1996b, AJ, 112, 2596

Gallart, C., Aparicio, A., & Vilchez, J. M. 1996c, AJ, 112, 1928

Gallart, C., Freedman, W., Mateo, M., Chiosi, C., Thompson, I., Aparicio, A., Bertelli, G., Hodge, P., Lee, M., Olszewski, E., Saha, A., Stetson, P., & Suntzeff, N. 1999, ApJ, 514, 665

Gordon, D., & Gottesman, S. T. 1981, AJ, 86, 161

Greggio, L., Marconi, G., Tosi, M., & Focardi, P. 1993, AJ, 105, 894

Greggio, L., Tosi, M., Clampin, M., de Marchi, G., Leitherer, C., Nota, A., & Sirianni, M. 1998, ApJ, 504, 725

Hidalgo, S. L., Marin-Franch, A., & Aparicio, A. 2003a, AJ, 124, 1247

Hidalgo, S. L., Marín-Franch, A., & Aparicio, A. 2003b, AJ, 125, 1247

Hodge, P. W. 1971, ARA&A, 9, 35

Hodge, P. W., & Hitchcock, J. L. 1966, PASP, 78, 79

Holmberg, E. 1958, Medd. Lunds Astr. Obs., 2, No. 136, 91

Huchtmeier, W. K., Hopp, U., & Kuhn, B. 1997, A&A, 319, 67

Huchtmeier, W. K., Seiradakis, J. H., & Materne, J. 1981, A&A, 102, 134

Hunter, D. A. 2001, ApJ, 559, 225

Hunter, D. A., & Elmegreen, B. G. 2004, AJ, 128, 2170

Hunter, D. A., Elmegreen, B. G., & Anderson, E. 2006, in preparation

Hunter, D. A., Elmegreen, B. G., & Baker, A. L. 1998, ApJ, 493, 595

Hunter, D. A., Elmegreen, B. G., van Woerden, H. 2001a, ApJ, 556, 773

Hunter, D. A., & Gallagher, J. S. 1985a, AJ, 90, 1457

Hunter, D. A., & Gallagher, J. S. 1985b, AJ, 90, 1789

Hunter, D. A., & Gallagher, J. S. 1986, PASP, 98, 5

Hunter, D. A., Gallagher, J. S., & Rautenkranz, D. 1982, ApJS, 49, 53

Hunter, D. A., & Hoffman, L. 1999, AJ, 117, 2789

Hunter, D.A., Hunsberger, S.D., & Roye, E.W. 2000, ApJ, 542, 137

Hunter, D. A., et al. 2001b, ApJ, 553, 121

Hunter, D. A., & Plummer, J. 1996, ApJ, 462, 732

Hunter, D. A., Rubin, V. C., Swaters, R. A., Sparke, L. S., & Levine, S. E. 2002, ApJ, 580, 194

Hunter, D. A., van Woerden, H., & Gallagher, J. S. 1999, AJ, 118, 2184

Hunter, D. A., & Wilcots, E. M. 2002, AJ, 123, 2449

Israel, F. P. 1988, ApJ, 344, 685

Karachentsev, I. D., Aparicio, A., & Makarova, L. 1999, A&A, 352, 363

Karachentsev, I. D., Musella, I., & Grimaldi, A. 1996, A&A, 310, 722

Karachentsev, I. D., et al. 2002, A&A, 383, 125

Karachentsev, I. D., et al. 2003a, A&A, 398, 467

Karachentsev, I. D., et al. 2003b, A&A, 398, 479

Kennicutt, R. C., Jr. 1983, ApJ, 272,54

Kennicutt, R. C., Jr. 1989, ApJ, 344, 685

Kniazen, A. Y., et al. 2000, A&A, 357, 101

Kregel, M., & van der Kruit, P. C. 2004, MNRAS, 355, 143

Kregel, M., van der Kruit, P. C., & de Grijs, R. 2002, MNRAS, 334, 646

Kunth, D. 1985, in Star-Forming Dwarf Galaxies edited by D. Kunth, T. X. Thuan, & J. T. Thanh Van, (France:Editions Frontieres), p. 183

Kunth, D. 1987, in Chemical evolution of galaxies with active star formation: Proceedings of the Japan-France Seminar (Tokyo, Universal Academy Press, Inc.), 187

Lake, G., & Skillman, E. D. 1989, AJ, 98, 1274

Landolt, A. U. 1992, AJ, 104, 340

Lee, M. G., Aparicio, A., Tikhonov, N., Byun, Y.-I., & Kim, E. 1999, AJ, 118, 853

Lee, M. G., & Kim, S. C. 2000, AJ, 119, 777

LeLièvre, M., & Roy, J.-R. 2000, AJ, 120, 1306

Lo, K. Y., Sargent, W. L. W., & Young, K. 1993, AJ, 106, 507

MacArthur, L. A., Courteau, S., & Holtzman, J. A. 2003, ApJ, 582, 689

MacArthur, L. A., Courteau, S., Bell, E., & Holtzman, J. A. 2004, ApJS, 152, 175

Mac Low, M.-M., Klessen, R. S. 2004, RevModPhy, 76, 125

Maiz-Apellaniz, J., Cieza, L., & Mackenty, J. W. 2002, AJ, 123, 1307

Makarova, L. N. 1999, A&AS, 139, 491

Makarova, L. N., Karachentsev, I. D., Grebel, E. K., & Barsunova, O. Y. 2002, A&A, 384, 72

Makarova, L. N., Karachentsev, I. D., Takalo, L. O., Heinaemaeki, P., & Valtonen, M. 1998, A&AS, 128, 459

Marconi, G., Tosi, M., Greggio, L, & Focardi, P. 1995, AJ, 109, 173

Martin, C. L., & Kennicutt, R. C., 2001, ApJ, 555, 301

Massey, P., & Armandroff, T. E. 1995, AJ, 109, 2470

Méndez, B., Davis, M., Moustakas, J., Newman, J., Madore, B. F., & Freedman, W. L. 2002, AJ, 124, 213

Meurer, G. R., Carignan, C., Beaulieu, S. F., & Freeman, K. C. 1996, AJ, 111, 1551

Meurer, G. R., Staveley-Smith, L., & Killeen, N. E. B. 1998, MNRAS, 300, 705

Miller, B. W., Dolphin, A. E., Lee, M. O., Kim, S. C., & Hodge, P. 2001, ApJ, 562, 713

Minniti, D., & Zijlstra, A. A. 1996, ApJ, 467, L13

Minniti, D., & Zijlstra, A. A. 1997, AJ, 114, 147

Minniti, D., Zijlstra, A. A., & Alonso, M. V. 1999, AJ, 117, 881

Noeske, K. G., Papaderos, P., Cairós, L. M., & Fricke, K. J. 2003, A&A, 410, 481

Nordgren, T. E., et al., 2003, private communication

O'Connell, R. W., Gallagher, J. S., III, Hunter, D. A. 1994, ApJ, 433, 65

Papaderos, P., Loose, H.-H., Fricke, K. J., & Thuan, T. X. 1996, A&A, 314, 59

Parodi, B. R., Barazza, F. D., & Binggeli, B. 2002, A&A, 388, 29

Patterson, R. J., & Thuan, T. X. 1996, ApJS, 107, 103

Pérez, I. 2004, A&A, 427, L17

Phillipps, S., Disney, M. J., Kibblewhite, E. J., & Cawson, M. G. M. 1987, MNRAS, 229, 505

Pildis, R. A., Schombert, J. M., & Eder, J. A. 1997, ApJ, 481, 157

Pohlen, M., Beckman, J. E., Hüttemeister, S., Knapen, J. H., Erwin, P., & Dettmar, R.-J. 2004, astroph/0405541

Pohlen, M., Dettmar, R.-J., Lütticke, R., & Aronica, G. 2002, A&A, 392, 807

Puche, D., Westpfahl, Brinks, E., & Roy, J-R. 1992, AJ, 103, 1841

Quirk, W. J. 1972, ApJ, 176, L9

Roberts, M. S., & Haynes, M. P. 1994, ARA&A, 32, 115

Rocha-Pinto, H. J., Maciel, W. J., Scalo, J., & Flynn, C. 2000, A&A, 358, 850

Roye, E. W., & Hunter, D. A. 2000, AJ, 119, 1145

Safronov, V. S. 1960, Ann.d'Ap., 23, 979

Sargent, W. L. W., Sancisi, R., & Lo, K. Y. 1983, ApJ, 265, 711

Sargent, W. L. W., & Searle, L. 1970, ApJ, 162, L155

Schaye, J. 2004, ApJ, 609, 667

Shostak, G. S., & van der Kruit, P. C. 1984, A&A, 132, 20

Simon, J. D., Bolatto, A. D., Leroy, A., & Blitz, L. 2003, ApJ, 596, 957

Simpson, C. E., Hunter, D. A., & Knezek, P. M. 2005a, AJ, 129, 160

Simpson, C. E., Hunter, D. A., & Nordgren, T. E. 2005b, AJ, Sept

Skillman, E. D., Terlevich, R., Teuben, P. J., & van Woerden, H. 1988, A&A, 198, 33

Stanimirovic, S., Staveley-Smith, L., Dickey, J.M., Sault, R.J., & Snowden, S.L. 1999, MN-RAS, 302, 417

Staveley-Smith, L., Davies, R. D., & Kinman, T. D. 1992, MNRAS, 258, 334

Stil, J. M., & Israel, F. P. 2002, A&A, 389, 29

Sung, E.-C., Han, C., Ryden, B. S., Patterson, R. J., Chun, M.-S., Kim, H.-I., Lee, W.-B., & Kim, D.-J. 1998, ApJ, 505, 199

Swaters, R. A. 1999, Ph.D. thesis, Rijksuniversiteit Groningen

Swaters, R. A., & Balcells, M. 2002, A&A, 390, 863

Telles, E., Melnick, J., & Terlevich, R. 1997, MNRAS, 288, 78

Thuan, T. X., Izotov, Y., & Foltz, C. B. 1999, ApJ, 525, 105

Thuan, T. X., & Martin, G. E. 1981, ApJ, 247, 823

Tolstoy, E. 1996, PhD thesis, Rijksuniversiteit Groningen

Tolstoy, E., Gallagher, J. S., Cole, A. A., Hoessel, J. G., Saha, A., Dohm-Palmer, R. C., Skillman, E. D., Mateo, M., & Hurley-Keller, D. 1998, AJ, 116, 1244

Tolstoy, E., Saha, A., Hoessel, J. G., & Danielson, G. E. 1995, AJ, 109, 579

Toomre, A. 1964, ApJ, 139, 1217

Tosi, M., Greggio, L., Marconi, G., & Focardi, P. 1991, AJ, 102, 951

Tosi, M., Sabbi, E., Bellazzini, M., Aloisi, A., Greggio, L., Leitherer, C., & Montegriffo, P. 2001, AJ, 122, 1271

van den Bergh, S. 1988, PASP, 100, 344

van der Hulst, J. M., Skillman, E. D., Smith, T. R., Bothun, G. D., McGaugh, S. S., & De Blok, W. J. G. 1993, AJ, 106, 548

van der Kruit, P.C. 1987, A&A, 173, 59

van der Kruit, P.C. 1988, A&A, 192, 117

van der Kruit, P.C. 1989, in The Milky Way as a Galaxy, ed. R. Buser & I. R. King (Mill Valley, CA:Univ. Science Books), p 257

van der Kruit, P. C., & Shostak, G. S. 1982, A&A, 105, 351

van Zee, L. 2000, AJ, 119, 2757

van Zee, L., Haynes, M. P., & Giovanelli, R. 1995, AJ, 109, 990

van Zee, L., Haynes, M. P., Salzer, J. J., & Broeils, A. H. 1997a, AJ, 113, 1618

van Zee, L., Maddalena, R. J., Haynes, M. P., Hogg, D. E., & Roberts, M. S. 1997b, AJ, 113, 1638

Westpfahl, D.J., Coleman, P.H., Alexander, J., Tongue, T. 1999, AJ, 117, 868

Willett, K. W., Elmegreen, B. G., & Hunter, D. A. 2005, AJ, 129, 2186

Wolfire, M. G., McKee, C. F., Hollenbach, D., & Tielens, A. G. G. M. 2003, ApJ, 587, 278

Young, L. M., & Lo, K. Y. 1997, ApJ, 490, 710

Youngblood, A. J., & Hunter, D. A. 1999, ApJ, 519, 55

This preprint was prepared with the AAS IATEX macros v5.2.

Table 1. Galaxy Sample

Galaxy	Other Names <sup>a</sup>	$\mathrm{Type^{b}}$	D (Mpc)	Ref. <sup>c</sup>	$\mathrm{E}(\mathrm{B}\mathrm{-V})_f{}^{\mathrm{d}}$	$\log \mathrm{M}_{gas}^{\mathrm{e}}$ $(\mathrm{M}_{\odot})$	Ref.f			
Im Galaxies										
A1004+10	PGC 29428, UGC 5456, IRAS F10046+1036	I0?	6.5		0.01	7.59	23			
A2228+33	PGC 69019, UGC 12060, IRAS F22282+3334	$_{\mathrm{IBm}}$	16.9		0.01	9.35	22			
CVnIdwA	UGCA 292	Im?	4.1	27	0.01	7.92	51			
D508-2	LSBC F508-V01	Im	29.9		0.00	9.18	42			
D575-5	LSBC F575-03	$\mathrm{d}\mathrm{I}$	6.2		0.03	7.52	42			

Note. — Table 1 is published in its entirety in the electronic edition of the *Astrophysical Journal*. A portion is shown here for guidance regarding its form and content.

References. — (1) Allsopp 1978; (2) Aparicio 1994; (3) Aparicio, Tikhonov, & Karachentsev 2000; (4) Bottinelli et al. 1990; (5) Bureau & Carignan 2002; (6) Carignan & Beaulieu 1989; (7) de Blok, McGaugh, & van der Hulst 1996; (8) de Blok & Walter 2000; (9) Dohm-Palmer et al. 1998; (10) Dolphin 2000; (11) Dolphin et al. 2002; (12) Dolphin et al. 2003; (13) Fisher & Tully 1981; (14) Freedman et al. 2001; (15) Gallagher et al. 1998; (16) Gallart, Aparicio, & Vilchez 1996c; (17) Gordon & Gottesman 1981; (18) Hidalgo, Marín-Franch, & Aparicio 2003a; (19) Huchtmeier, Hopp, & Kuhn 1997; (20) Huchtmeier, Seiradakis, & Materne 1981; (21) Hunter 2001; (22) Hunter & Gallagher 1985b; (23) Hunter, Gallagher, & Rautenkranz 1982; (24) Karachentsev, Aparicio, & Makarova 1999; (25) Karachentsev, Musella, & Grimaldi 1996; (26) Karachentsev et al. 2002; (27) Karachentsev et al. 2003a; (28) Karachentsev et al. 2003b; (29) Kniazen et al. 2000; (30) Lee et al. 1999; (31) Lee & Kim 2000; (32) Lo, Sargent, & Young 1993; (33) Maiz-Apellaniz, Cieza, & Mackenty 2002; (34) Makarova et al. 1998; (35) Massey & Armandroff 1995; (36) Méndez et al. 2002; (37) Meurer, Staveley-Smith, & Killeen 1998; (38) Miller et al. 2001; (39) Minniti & Zijlstra 1997; (40) Nordgren et al., 2003; (41) O'Connell et al. 1994; (42) Pildis, Schombert, & Eder 1997; (43) RC3; (44) Sargent, Sancisi, & Lo 1983; (45) Stil & Israel 2002; (46) Swaters 1999; (47) Thuan & Martin 1981; (48) Tolstoy et al. 1995; (49) Tosi et al. 2001; (50) van Zee, Haynes, & Giovanelli 1995; (51) van Zee et al. 1997b; and (52) Young & Lo 1997.

<sup>&</sup>lt;sup>a</sup>Selected alternate identifications obtained from NED.

<sup>&</sup>lt;sup>b</sup>Morphological Hubble types are from de Vaucouleurs et al. (1991). If no type is given there, we have used types given by NED.

<sup>&</sup>lt;sup>c</sup>Reference for the distance to the galaxy. If no reference is given, the distance was determined from  $V_{GSR}$  given by de Vaucouleurs et al. (1991) and a Hubble constant of 65 km s<sup>-1</sup> Mpc<sup>-1</sup>.

<sup>&</sup>lt;sup>d</sup>Foreground reddening from Burstein & Heiles (1984).

<sup>&</sup>lt;sup>e</sup>The gas mass is the H I mass  $M_{HI}$  plus  $1.34 \times M_{HI}$  to account for He.

<sup>&</sup>lt;sup>f</sup>Reference from which the H<sub>I</sub> mass was taken. Masses were modified to reflect the distances used here as necessary.

- 43

Table 2. Observations and Photometry Parameters

	Ellipse photometry parameters <sup>a</sup>											
				$Exposures^{c}$	$Seeing^d$	Scale	P.A.		$\operatorname{Step}$	Center (	J2000)	Calib rms <sup>e</sup>
Galaxy	Date	Instr. <sup>b</sup>	Filters	(s)	(arcsec)	(arcsec)	(deg)	b/a	(arcsec)	R.A.	Decl.	(mag)
Im Galaxies												
A1004+10	9903	LO1.8m	BV	$3\times1200, 3\times900$	1.7,1.5	0.61	-33.3	0.63	9.1	10 07 19.6	10 21 47	0.07,0.04
A2228+33	9810	LO1.1m	BV	$3 \times 2400, 3 \times 1200$	3.6, 3.0	1.13	38.5	0.92	11.3	$22\ 30\ 34.0$	$33\ 49\ 14$	0.03, 0.03
	9910	LO1.1m	U	$3 \times 2400$	3.4	1.13						0.05
CVnIdwA	0005	LO1.1m	UBV	$3 \times 1800, 8 \times 900, 9 \times 600$	3.8,3.9,2.8	1.13	79.5	0.78	11.3	$12\ 38\ 40.2$	$32\ 45\ 40$	0.04,0.03,0.02
D508-2	0004	LO1.1m	UBV	$4 \times 1800, 3 \times 1800, 7 \times 1200$	3.8,3.8,3.1	1.13	70.6	0.76	9.1	13 04 34.3	$26\ 46\ 24$	0.07,0.02,0.02
D575-5	9903	LO1.8m	BV	$4 \times 1800, 4 \times 900$	3.3,3.1	0.61	56.0	0.51	9.1	$12\ 55\ 41.0$	19 12 35	0.03, 0.04
	9904	LO1.8m	U	$2 \times 1800$	3.1	0.61						0.05

Note. — Table 2 is published in its entirety in the electronic edition of the Astrophysical Journal. A portion is shown here for guidance regarding its form and content.

<sup>a</sup>Position angle P.A., minor-to-major axis ratio b/a, ellipse semi-major axis step size, and position of center used to do photometry in concentric ellipses. The P.A. given here has been corrected for the P.A. of the CCD camera on the sky, usually about  $0.5^{\circ}$ , but the P.A. appropriate to the image itself was used for the photometry.

<sup>b</sup>Telescope used for the observations: LO1.8m=1.8 m Perkins Telescope at Lowell Observatory; LO1.1m=1.1 m Hall Telescope at Lowell Observatory; KPNO4m=Kitt Peak National Observatory 4 m Telescope; CTIO1.5m=Cerro Tololo Inter-American Observatory 1.5 m Telescope; CTIO5c=Cerro Tololo Inter-American Observatory Schmidt Telescope; CTIO4m=Cerro Tololo Inter-American Observatory 4 m Telescope.

<sup>&</sup>lt;sup>c</sup>A () designates images taken under clear sky conditions to calibrate the other frames taken under non-photometric conditions.

<sup>&</sup>lt;sup>d</sup>FWHM of a stellar profile on the final combined image.

<sup>&</sup>lt;sup>e</sup>Photometric calibration rms for the filters listed in Column 4.

-44

Table 3. Integrated Photometry

Galaxy	R <sup>b</sup> (arcmin)	$\mathrm{M}_{V_0}$	$\sigma_{M_V}$	(U-B) <sub>0</sub>	$\sigma_{U-B}$	(B-V) <sub>0</sub>	$\sigma_{B-V}$	(V-J) <sub>0</sub>	$\sigma_{V-J}$	(J-H) <sub>0</sub>	$\sigma_{J-H}$	(H-K) <sub>0</sub>	$\sigma_{H-K}$
						Im Galaxie	s						
A1004+10	0.33	-15.178	0.001			0.286	0.001						
	1.37	-15.930	0.001			0.326	0.001						
A2228+33	0.70	-17.002	0.008	-0.062	0.016	0.502	0.012						
	2.46	-17.754	0.013	-0.098	0.027	0.510	0.020						
CVnIdwA	0.56	-11.902	0.070	-0.675	0.102	0.096	0.091						
	1.32	-12.655	0.083	-0.551	0.142	0.207	0.111						
D508-2	0.32	-14.988	0.063	-0.661	0.116	-0.127	0.090						
	0.76	-15.742	0.072	-0.650	0.130	-0.127	0.101						
D575-5	0.49	-12.100	0.034	-0.282	0.055	0.159	0.039						
	0.91	-12.852	0.032	-0.137	0.053	0.199	0.037						

Note. — Table 3 is published in its entirety in the electronic edition of the Astrophysical Journal. A portion is shown here for guidance regarding its form and content.

 $<sup>^{\</sup>mathrm{a}}$ These values are V-H rather than V-J.

<sup>&</sup>lt;sup>b</sup>Integrated photometry is given at  $\mathbf{R}_{1/2}^V$  and the total extent of the V-band image, as well as the total extents in JHK.

Table 4. Structural Parameters

$Primary^a$						Secondary <sup>a</sup>								
Galaxy	$R_D$ (kpc)	$\sigma_{R_D}$ (kpc)	$\mu_0$ (mag arcsec <sup>-2</sup> )	$\sigma_{\mu_0}$ (mag arcsec <sup>-2</sup> )	Sec?b	$R_{Br}$ (kpc)	$R_D$ (kpc)	$\sigma_{R_D}$ (kpc)	$\mu_0$ (mag arcsec <sup>-2</sup> )	$\sigma_{\mu_0}$ (mag arcsec <sup>-2</sup> )	R <sub>25</sub> <sup>c</sup> (kpc)	$R_H^c$ (kpc)	$R_{1/2}^{V c}$ (kpc)	$\sigma_R^{\mathrm{d}}$ (kpc)
Im Galaxies														
A1004+10	0.34	0.01	20.37	0.12	N						1.28	1.83	0.62	0.08
A2228+33	2.56	0.11	22.85	0.09	N						3.82	7.39	3.44	0.23
CVnIdwA	0.64	0.15	24.30	0.26	N							1.04	0.67	0.06
D508-2	1.80	0.17	24.02	0.21	N						1.93	4.80	2.80	0.36
D575-5	0.85	0.12	24.69	0.15	N							1.27	0.89	0.07

Note. — Table 4 is published in its entirety in the electronic edition of the Astrophysical Journal. A portion is shown here for guidance regarding its form and content.

45

<sup>a</sup>Entries on the first line for a galaxy are measured from the V-band. Entries on a second line, if present, are measured from the J-band image. The exception are the "Other Objects," which are measured only in J-band.

<sup>b</sup>If the surface photometry was fit with two parts it is noted here as inward of the primary fit ("1") or outward ("0"). The parameter  $R_{Br}$  is the radius at which the two fits cross each other. An "N" means that the surface photometry was fit with only one exponential.

 $^{c}$ R<sub>25</sub> and R<sub>H</sub> are measured from reddening-corrected B-band surface photometry. R $_{1/2}^{V}$  is measured from the reddening-corrected V-band surface photometry.

<sup>d</sup>The uncertainty in  $R_{25}$ ,  $R_H$ , and  $R_{1/2}^V$  is one-quarter of the annulus width in the ellipse photometry from which these quantities were determined. A minimum of 2.5" is imposed, comparable to the average seeing.

Table 5. Disk Characteristics

					I	$\mathrm{Bar^d}$			$\mu_{25}{}^{\mathrm{f}}$	$\sigma_{\mu_{25}}$	$\mu_D^{V\mathrm{f}}$	$\sigma_{\mu_D^V}$	$\mu_{2.5D}{}^{\mathrm{f}}$	$\sigma_{\mu_{2.5D}}$
Galaxy	$i^{\rm a}$ (deg)	Complex $\mu_V$ ? <sup>b</sup>	Pec?c	$R_{Bar}$ (kpc)	$\mathbf{R}_{Bar}/\mathbf{R}_{D}^{V}$	b/a	$\Delta$ P.A. (deg)	$\Delta {\rm R}/{\rm R}_D^{V{\rm e}}$	$(\text{mag}\ \text{arcsec}^{-2})$	$(\text{mag} \\ \text{arcsec}^{-2})$	$(\text{mag} \\ \text{arcsec}^{-2})$	(mag	$(\text{mag} \\ \text{arcsec}^{-2})$	$(\text{mag} \\ \text{arcsec}^{-2})$
						Iı	n Galaxie	s						
A 1004 + 10	54		C						22.06	0.00	01 19	0.00	21.02	0.00
A1004+10 A2228+33	$\frac{54}{24}$	•••	_	2.18±0.43	0.8	0.69	 78	0.00	22.86 $24.12$	$0.00 \\ 0.01$	21.13 $23.17$	0.00 $0.00$	21.93 $24.29$	0.00
CVnIdwA	40			2.10±0.45	0.8	0.09		0.00	24.12	0.01	25.17	0.00 $0.07$	24.29	0.01
D508-2	42								24.80	0.08	24.89	0.08	25.55	0.06
D575-5	64										25.43	0.03		

Note. — Table 5 is published in its entirety in the electronic edition of the *Astrophysical Journal*. A portion is shown here for guidance regarding its form and content.



<sup>&</sup>lt;sup>a</sup>The inclination of the galaxy, determined from the b/a in Table 2 under the assumption that  $(b/a)_0 = 0.3$  for the irregulars and 0.2 for the spirals.

<sup>&</sup>lt;sup>b</sup>If a galaxy has a complex  $\mu_V$ , it is marked as FI="flat inner part", FO="flat outer part", SO="steeper outer part", SI="steeper inner part"

<sup>&</sup>lt;sup>c</sup> "M" indicates the presence of a morphological peculiarity, and "C", the presence of a color peculiarity.

<sup>&</sup>lt;sup>d</sup>Characteristics of a bar structure, if present, are given.  $R_{Bar}$  is the semi-major axis length of the bar. This quantity is followed by a "?" if there is some question as to whether what is seen is a bar structure. The uncertainty is the maximum amount by which we feel that the bar length could reasonably be altered based on contour plots. b/a is the minor to major axis ratio of the bar.  $\Delta P.A$ . is the difference in the position angle between the bar and the outer galaxy. If no value is given, the outer galaxy was too round to reliably determine the P.A.

<sup>&</sup>lt;sup>e</sup>Radial separation between center of bar and center of outer isophotes in the plane of the galaxy as determined in the V-band relative to the scale-length  $R_D^V$  of the disk. An offset less than the seeing of the boxcar-smoothed image was set to zero.

 $<sup>^{\</sup>mathrm{f}}\mu_{25}$ ,  $\mu_{D}^{V}$ , and  $\mu_{2.5D}$  are the average surface brightnesses, magnitudes in 1 arcsec<sup>2</sup>, within the radii  $\mathrm{R}_{25}$ ,  $\mathrm{R}_{D}^{V}$ , and  $2.5\times\mathrm{R}_{D}^{V}$ , respectively.  $\mu_{25}$  is measured on the B-band image, and  $\mu_{D}^{V}$  and  $\mu_{2.5D}$ , on the V-band image. The photometry is normalized to the circular area, that is,  $\pi\mathrm{R}^{2}$ .

Table 6. Color gradients

				Part 1 <sup>a</sup>		Part 2 <sup>a</sup>					
Galaxy	Color	$R_{beg}^{\ b}$ (kpc)	$R_{end}^{b}$ (kpc)	Gradient (mag/kpc)	$\sigma_{grad}$ (mag/kpc)	$R_{beg}^{b}$ (kpc)	$R_{end}^{b}$ (kpc)	Gradient (mag/kpc)	$\sigma_{grad}$ (mag/kpc)		
Im Galaxies											
A1004+10	$\mathrm{B}\mathrm{-V}$	0.00	1.01	0.0	0.0	1.01	2.44	0.339	0.026		
DDO 24	B-V	0.00	3.86	-0.071	0.002						
	U-B	0.00	3.27	-0.060	0.012						
DDO 25	$\mathrm{B}\mathrm{-V}$	0.00	4.54	-0.034	0.005						
DDO 34	U-B	0.00	2.65	-0.200	0.016						
DDO 38	$\mathrm{B}\mathrm{-V}$	0.00	5.61	-0.052	0.004						
	U-B	0.00	5.61	-0.074	0.015						

Note. — Table 6 is published in its entirety in the electronic edition of the  $Astrophysical\ Journal$ . A portion is shown here for guidance regarding its form and content.

<sup>&</sup>lt;sup>a</sup>Surface photometry profiles for some galaxies were fit with two gradients with different slopes.

 $<sup>^{\</sup>mathrm{b}}\mathrm{The}$  range of radii over which the gradient was measured.

Table 7. Median disk parameters.

Parameter	Im	BCD	Sm
$\mu_0^V \text{ (mag of 1 arcsec}^2\text{)}$	23.1	21.0	22.2
$\mu_0^J \text{ (mag of 1 arcsec}^2)$ $R_D^V \text{ (kpc)}$	21.2 $1.0$	$19.9 \\ 0.5$	$\frac{20.2}{1.7}$
$R_D^J$ (kpc)	0.7	0.4	1.3
$b/a \ { m M}_{V_0}$	0.6 -15.4	0.6 $-16.0$	0.7 $-17.4$
$R_{1/2}^V$ (kpc)	1.4	0.8	3.0
$\mu_{25}$ (mag of 1 arcsec <sup>2</sup> )	24.4	23.1	24.1
$\mu_{25}$ (mag of 1 arcsec <sup>2</sup> ) $\mu_D^V$ (mag of 1 arcsec <sup>2</sup> )	$24.4 \\ 24.0$	23.1 $21.4$	24.1 23.0

Table 8. Average characteristics of two-part surface brightness profiles.

Type	No.	Percent	$R_{Br}/R_H$	$R_{Br}/R_{1/2}^V$	$R_{Br}/R_D^{Va}$	$\mathbf{R}^{V}_{D,i}/\mathbf{R}^{V}_{D,o}{}^{\mathrm{b}}$				
Exponential becomes steeper										
Im	11	12	$0.8 \pm 0.3$	$1.4 \pm 0.3$	$1.5 \pm 0.8$	$2.5 \pm 0.6$				
$\operatorname{Sm}$	8	44	$0.7 \pm 0.1$	$1.5 \pm 0.1$	$2.2 \pm 0.5$	$1.9 \pm 0.3$				
Exponential becomes shallower										
Im	3	3	$0.6 \pm 0.3$	$1.3 \pm 0.5$	$1.7 \pm 1.0$	$0.6 \pm 0.2$				
BCD	8	33	$0.6 \pm 0.1$	$1.9 \pm 0.3$	$2.0 \pm 0.5$	$0.6 \pm 0.1$				
			Flat inn	er profile						
Im	8	9	$0.5 \pm 0.1$	$0.8 \pm 0.2$	$1.6 \pm 0.7$					
BCD	2	8	$0.4 \pm 0.3$	$0.8 \pm 0.4$	$1.9 \pm 1.3$	• • •				
			Flat out	er profile						
Im	1	1	$0.4 \pm 0.3$	$0.8 \pm 0.4$	1.9±1.3					

 $<sup>{}^{\</sup>rm a}{\rm R}^V_D$  is the scale-length of the inner V-band profile for the exponential that becomes steeper in the outer parts and of the outer profile for the exponential that is shallower in the outer parts.

<sup>&</sup>lt;sup>b</sup>Ratio of inner scale-length  $\mathbf{R}_{D,i}^V$  to the outer scale-length  $\mathbf{R}_{D,o}^V$ .

Fig. 1.— False-color display of an example of the dataset using the Im galaxy NGC 2366. Upper: The logarithms of the V-band and H $\alpha$  images are shown in order to allow comparison of faint outer features and bright inner features. Lower left: A composite of the UBV images, with V as red, B as green, and U as blue. Lower right: A composite of the JHK images, with K as red, H as green, and J as blue. North is at the top; East is to the left.

Fig. 2.— Azimuthally-averaged V-band, J-band, and H $\alpha$  surface photometry of NGC 2366, an example of our surface photometry data set. All are corrected for reddening. The scales for  $\Sigma_{H\alpha}$ ,  $\mu_{V_0}$ , and  $\mu_{J_0}$  have been set so that they cover the same logarithmic interval. The solid lines are fits to the V and J-band surface photometry. The radii corresponding to  $R_{25}$  and  $R_H$  are marked with vertical lines near the bottom of the plot. The deviations in the surface photometry of NGC 2366 near 1 kpc radius are due to the supergiant H II region NGC 2363.

Fig. 3.— As for Figure 2, but showing the azimuthally-averaged colors. The solid line in each panel is the average color of points with relatively low uncertainties. The deviations in the colors of NGC 2366 near 1 kpc radius are due to the supergiant H II region NGC 2363.

Fig. 4.— Cuts along the major axis through the V-band image of DDO 48 illustrate the sky background and the location of the breaks in the surface photometry profile without azimuthal averaging. In the top panel a cut through the sky-subtracted image is shown; the cut sums over 11 pixels (12.5") and then is averaged along the cut in 10 pixel increments. The magnitude is on an arbitrary scale, formed from the counts in the image plus a constant of 25. The vertical lines mark the center of the image (dashed line) and the break radius (solid lines). The solid sloped lines are the fits to the azimuthally-averaged surface photometry used elsewhere in this paper, and anchored on this plot at the first point in the radial interval of that portion of the double exponential. The radial interval plotted here also corresponds to that plotted in the azimuthally-averaged surface brightness plot of this galaxy. The bottom panel shows a similar cut through the original V-band image, and the dashed line is this cut through the two-dimensional fit to the sky. These are plotted as counts rather than as magnitudes, and here the cut spans the entire V-band image. The small bottom-most panel is the cut through the sky-subtracted image, shown as counts rather than as magnitudes and displayed to view the background level after sky-subtraction. The portion of the galaxy corresponding to the outer exponential stands clearly above the sky noise.

Fig. 5.— Number distribution of the survey galaxies in integrated  $M_V$ , corrected for reddening. The vertical dashed line marks the median value in  $M_{V_0}$  for the Im galaxies. Spiral galaxies from the sample of Kennicutt (1983) are shown for comparison.

Fig. 6.— Number distribution of the survey galaxies in  $\mu_{25}$ , the average surface brightness within a B-band isophote of 25 mag in one arcsec<sup>2</sup>, corrected for reddening. The dashed vertical line marks the median value of  $\mu_{25}$  for the Im group. Spiral galaxies from the sample of Kennicutt (1983) are shown for comparison and have been corrected to normalization by the circular area  $\pi R^2$ .

Fig. 7.— Number distribution of the survey galaxies in  $\mu_D^V$ , the average surface brightness within  $\mathcal{R}_D^V$  in V-band, corrected for reddening. The dashed vertical line marks the median value of  $\mu_D^V$  for the Im group.

Fig. 8.— Number distribution of the survey galaxies in  $R_{1/2}^V$ , the radius that contains half of the light of the galaxy in V-band. The dashed vertical line marks the median value of  $R_{1/2}^V$  for the Im group.

Fig. 9.— Number distribution of the barred survey galaxies in semi-major axis length of the bar  $R_{Bar}$  relative to the disk scale-length  $R_D^V$ .

Fig. 10.— Profile cuts along the major and minor axes of the bars in 6 of the survey galaxies. The three galaxies in the top row are the only barred systems in our survey showing a flat bar profile. The three galaxies in the bottom row are examples of the rest of the barred systems which show an exponential bar profile. The plots are centered on the center of the bar as determined in the V-band image. The cuts average over 5". The  $\mu_V$  have not been corrected for reddening.

Fig. 11.— Comparison of properties for barred (hatch at PA 45°) and non-barred (hatch at PA  $-45^{\circ}$ ) Im galaxies showing the influence of bars on star formation and surface brightness. The star formation rate (SFR<sub>D</sub>; from Hunter & Elmegreen 2004) is the integrated rate normalized to the area  $\pi R_D^2$ . The quantity  $\mu_D^V$  is the average V-band surface brightness within  $R_D^V$ .  $R_{HII}/R_D^V$  is the radius at which the furthest H II region is found in the disk, relative to  $R_D^V$ . The barred Ims have higher star formation rates, higher central surface brightnesses, and larger radial extents of the H II regions than the non-barred Ims. This figure appears in color in the electronic version of the Astrophysical Journal.

Fig. 12.— Number distribution of galaxies in the sample with a given projected minor-to-major axis ratio b/a. The vertical dashed line marks the median value in b/a for the Im sample.

Fig. 13.— A model for the distribution of the apparent ratio of axes for randomly projected triaxial galaxies with an intrinsic width to length ratio uniformly distributed between 0.7 and 1, and an intrinsic thickness to length ratio uniformly distributed between 0.29 and 0.67.

Fig. 14.— (top) Average surface brightness  $\mu_{2.5R_D}$  within a radius of  $2.5R_D^V$  in V-band as a function of the minor-to-major axis ratio of the galaxy. The normalizing area is the area of the ellipse, not the circular area in the plane of the galaxy as used for  $\mu_{2.5D}$  in Table 5. The lines indicate median values in b/a bins of 0.1 width. There is no correlation but the galaxies with the faintest surface brightnesses tend to lie near the peak in the overall distribution of b/a. (bottom) Absolute V-band magnitude versus axial ratio, showing a general brightening of all galaxy types for increasing b/a. This figure appears in color in the electronic version of the Astrophysical Journal.

Fig. 15.— (top) Distribution of  $2.5R_D^V$  in kpc is shown versus axial ratio for the three galaxy types. The lines indicate median values in b/a bins of 0.1 width. There is no significant trend. (bottom) Integrated color versus axial ratio, with a trend toward redder colors for more circular projected shapes in the case of BCD galaxies. This figure appears in color in the electronic version of the *Astrophysical Journal*.

Fig. 16.— Integrated UBV colors of our survey galaxies. Average colors are shown for spiral galaxies (de Vaucouleurs & de Vaucouleurs 1972). The UBV colors are corrected for reddening using the foreground reddening of Burstein & Heiles (1984), an assumed internal reddening of  $E(B-V)_i = 0.05$ , and the reddening law of Cardelli et al. (1989).

Fig. 17.— Integrated JHK colors of our survey galaxies corrected for reddening. For comparison, several spirals, an H II region, and a globular cluster that we observed are shown as well. The average JHK colors of a sample of Im galaxies observed by Fioc & Rocca-Volmerange (1999) falls in the middle of this diagram (J-H=0.6, H-K=0.2). The error bars for the spiral and globular cluster colors are the size of the plotted points and are not drawn.

Fig. 18.— Integrated VJH colors of our survey galaxies corrected for reddening.

Fig. 19.— Azimuthally-averaged colors as a function of radius in the Sm galaxy NGC 2552. Solid lines are fits to color gradients. This is an example of complex color profiles, seen in U–B and B–V, and the uncorrelated nature of the different colors.

Fig. 20.— B–V color gradients normalized to the disk scale-length  $R_D^V$  plotted against the integrated absolute V magnitude of the galaxy (top), the central V-band surface brightness from the exponential disk fit  $\mu_0^V$  (middle), and the disk scale-length  $R_D^V$  (bottom). Black symbols are the second part to two-part color profiles.

Fig. 21.— Colors for integrated stellar populations from the Bruzual & Charlot (2003) models. Decaying single population models are on the left and models with exponentially decaying star formation rates beginning 10 Gyr ago are on the right. The decay times are on the abscissa.

Fig. 22.— B/V images of NGC 2366 (top) and NGC 4449 (bottom). Black denotes a higher B/V ratio, or bluer colors. In these two galaxies there is a blue ridge that crosses the rectangular or boxy part of the galaxy from one corner to the other. North is at the top and East to the left.

Fig. 23.— Number distribution of galaxies in the sample with a given scale-length  $R_D^V$  from fits to the V-band radial surface photometry profiles. The vertical dashed line denotes the median value of  $R_D^V$  for the Im sample.

Fig. 24.— Number distribution of galaxies in the sample with a given central surface brightness  $\mu_0^V$  from fits to the V-band radial surface photometry profiles. The vertical dashed line denotes the median value of  $\mu_0^V$  for the Im sample.

Fig. 25.— V-band scale-length  $R_D^V$  versus J-band scale-length  $R_D^J$  from fits to the V-band and J-band surface photometry profiles. The solid line denotes equal values.

Fig. 26.— Scale-length  $R_D^V$  as a function of integrated  $M_{V_0}$  corrected for reddening (left) and central V-band surface brightness (right). The "de Jong spirals" are data from de Jong (1996a) and de Jong & van der Kruit (1994). The de Jong data were originally corrected for Galactic extinction, and we have corrected for internal extinction with an  $E(B-V)_i$  of 0.3 mag for each galaxy and no separate correction to face-on orientation.

Fig. 27.— (Top) Central surface brightness in V-band and (bottom) V-band disk scale-length versus galaxy type. The "de Jong spirals" are data from de Jong (1996a) and de Jong & van der Kruit (1994). The de Jong data were originally corrected for Galactic extinction. We have corrected for internal extinction with an  $E(B-V)_i$  of 0.3 mag for each galaxy. We plot our BCDs as galaxy type 11 in order to separate them from the Im systems. The horizontal lines through the Im, BCD, and Sm samples are the median values of  $\mu_0^V$  and  $R_D^V$  for our samples.

Fig. 28.— Central surface brightness in V-band versus integrated galaxy magnitude. The central surface brightness is for the primary exponential in those cases where the surface brightness is complex. The "de Jong spirals" are data from de Jong (1996a) and de Jong & van der Kruit (1994). The de Jong data were originally corrected for Galactic extinction. We have corrected for internal extinction with an  $E(B-V)_i$  of 0.3 mag for each galaxy. The average central surface brightness for spiral galaxies, from Freeman (1970), is indicated by the dashed line. Freeman's  $\mu_0^B = 21.65$  mag arcsec<sup>-2</sup> has been corrected for reddening in the same fashion that de Jong's spirals have been corrected ( $E(B-V)_i = 0.3$ ) and a  $(B-V)_0 = 0.6$  is used to convert  $\mu_0^B$  to  $\mu_0^V = 19.86$  mag arcsec<sup>-2</sup>. This figure appears in color in the electronic version of the Astrophysical Journal.

Fig. 29.— V-band surface brightness and B–V color profiles for Im galaxies with double exponential disks. Each galaxy is offset vertically for clarity and plotted with the same line color in the upper and bottom panels. The major ticmarks on the ordinate of the top panel correspond to 2 mag arcsec<sup>-2</sup>. The large ticmarks in the bottom panel correspond to 0.2 mag with red increasing towards the top. Galaxies that are identified in Table 5 as barred are marked with a "B" and those that are identified as having a peculiar morphology are marked with an "M." Profiles are labeled with the name of the galaxy, where DDO has been shortened to D, NGC to N, IC to I, and UGC to U.

Fig. 30.— As for Figure 29 but for the Sm galaxies with double exponential disks.

Fig. 31.— As for Figure 29 but for the galaxies with nearly uniform inner disks.



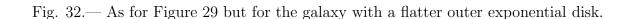


Fig. 33.— As for Figure 29 but for Im galaxies with shallower outer exponential profiles. IC 10 and NGC 3738 are very similar to BCD-type systems, shown in Figure 34, and like the BCDs have very blue inner disks due to intense, centrally concentrated star formation. This figure appears in color in the electronic version of the *Astrophysical Journal*.

Fig. 34.— As for Figure 29 but for BCD galaxies with shallower outer exponential profiles. All but Mrk 600 have very blue inner disks, indicative of central starbursts.

Fig. 35.— Ratio of the break radius  $R_{Br}$  to the main exponential scale-length  $R_D^V$  versus the V-band central surface brightness  $\mu_0^V$  for galaxies in our sample that have a double exponential surface brightness profile. Also shown are the four spirals from de Grijs et al. (2001) which have  $\mu_0^V$  (other studies used different pass-bands). Two of the de Grijs et al. spirals have break radii that are significantly different on the two sides of the galaxy. We have plotted these galaxies with the larger of the two radii.

Fig. 36.— V-band and H $\alpha$  surface brightness profiles are plotted with H I surface density profiles for survey galaxies with H I interferometric data in the literature. The quantities are plotted in equal log intervals. The line labelled R<sub>25</sub> marks the radius at which the B-band surface brightness profile reaches 25 magnitudes in 1 arcsec<sup>2</sup>, and R<sub>H</sub> marks the Holmberg radius. The solid line is a fit to the V-band surface photometry. The other lines just join the H $\alpha$  and H I surface brightness points, plotted as the logarithm. DDO 75, DDO 105, and DDO 168 show breaks in their surface brightness profiles. References for the H I are as follows: DDO 43—Simpson, Hunter, & Nordgren 2005; DDO 50—Puche et al. 1992; DDO 53—Nordgren et al. 2003; DDO 75—Skillman et al. 1988; DDO 88—Simpson, Hunter, & Knezek 2005; DDO 105—Broeils 1992; DDO 154—Carignan & Beaulieu 1989; DDO 155—Carignan et al. 1990; DDO 168—Broeils 1992; IC 1613—Lake & Skillman 1989; NGC 2366—Hunter, Elmegreen, & van Woerden 2001a; and UGC 199—Hunter & Wilcots 2002.

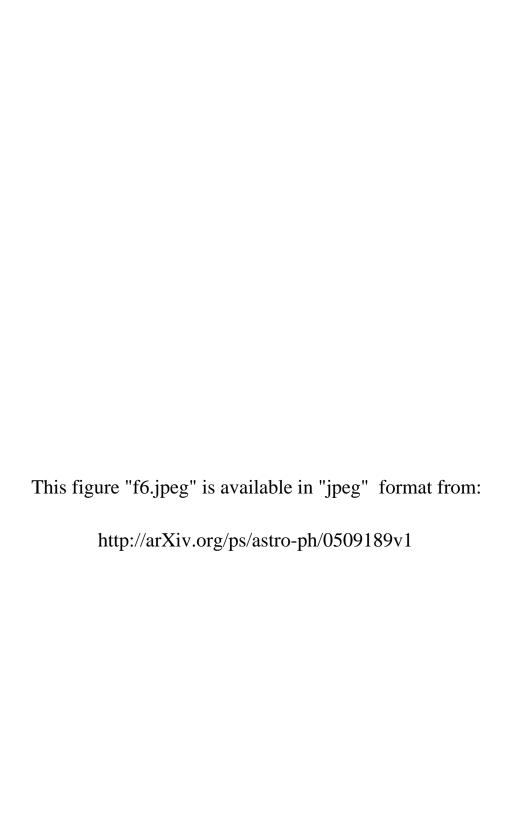
This figure "f1.jpeg" is available in "jpeg" format from:

This figure "f2.jpeg" is available in "jpeg" format from:

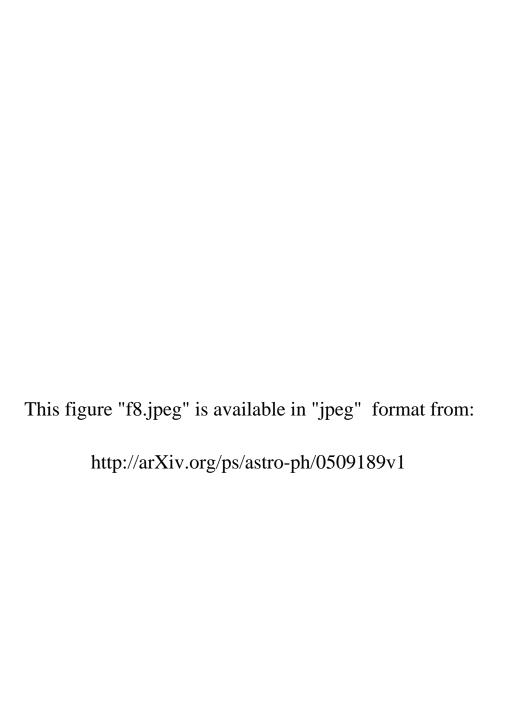
This figure "f3.jpeg" is available in "jpeg" format from:

This figure "f4.jpeg" is available in "jpeg" format from:

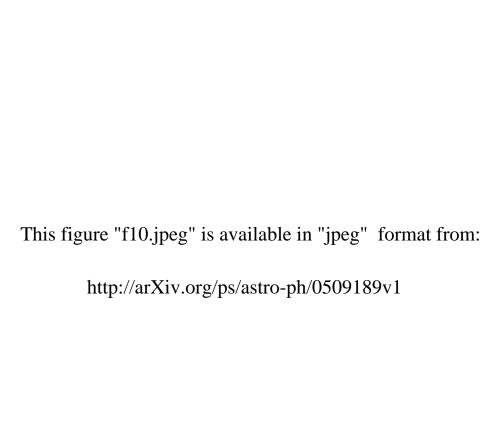
This figure "f5.jpeg" is available in "jpeg" format from:



This figure "f7.jpeg" is available in "jpeg" format from:



This figure "f9.jpeg" is available in "jpeg" format from:



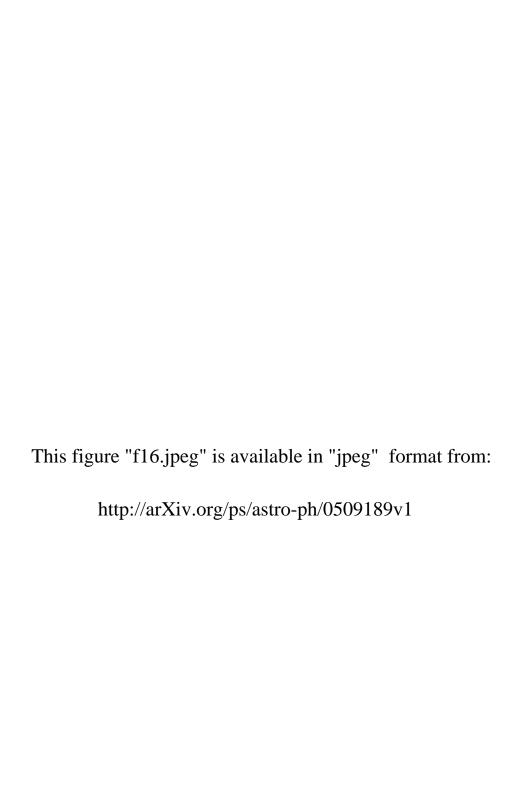
This figure "f11.jpeg" is available in "jpeg" format from:

This figure "f12.jpeg" is available in "jpeg" format from:

This figure "f13.jpeg" is available in "jpeg" format from:

This figure "f14.jpeg" is available in "jpeg" format from:

This figure "f15.jpeg" is available in "jpeg" format from:



This figure "f17.jpeg" is available in "jpeg" format from:

This figure "f18.jpeg" is available in "jpeg" format from:

This figure "f19.jpeg" is available in "jpeg" format from:

This figure "f20.jpeg" is available in "jpeg" format from:

This figure "f21.jpeg" is available in "jpeg" format from:

This figure "f22.jpeg" is available in "jpeg" format from:

This figure "f23.jpeg" is available in "jpeg" format from:

This figure "f24.jpeg" is available in "jpeg" format from:

This figure "f25.jpeg" is available in "jpeg" format from:

This figure "f26.jpeg" is available in "jpeg" format from:

This figure "f27.jpeg" is available in "jpeg" format from:

This figure "f28.jpeg" is available in "jpeg" format from:

This figure "f29.jpeg" is available in "jpeg" format from:

This figure "f30.jpeg" is available in "jpeg" format from:

This figure "f31.jpeg" is available in "jpeg" format from:

This figure "f32.jpeg" is available in "jpeg" format from:

This figure "f33.jpeg" is available in "jpeg" format from:

This figure "f34.jpeg" is available in "jpeg" format from:

This figure "f35.jpeg" is available in "jpeg" format from:

